

Endurance Testing and Fabrication of Advanced 15-cm and 30-cm Carbon-Carbon Composite Grids

Juergen Mueller*, John R. Brophy**, D.Kyle Brown***

*Jet Propulsion Laboratory
California Institute of Technology
Pasadena, CA 91109*

Two sets of carbon-carbon grids in a three-grid SAND configuration were endurance tested for 700 hours. Pre- and post test inspections employing electron microscope scans, x-ray fluorescence, grid mass loss measurements, and measurements of grid aperture diameters and thicknesses revealed an extraordinary low degree of erosion. No reduction in grid thicknesses was detectable within the margin of error of the measurements. Mass losses for the grids were on the order of 0.1 gm to 0.25 gm for the decelerator and accelerator grids, respectively and were attributed to an enlargement of grid apertures of 60 to 70 μ m for the accelerator grids. Grid permeance measurements were performed for two grid sets at various grid gap settings. Perveances obtained for carbon-carbon were slightly lower than those found for molybdenum grids which was attributed to a larger grid thickness of the carbon-carbon accelerator and decelerator grids. New, advanced carbon-carbon panels were fabricated with fiber volume fractions of up to 57% and flexural moduli approaching the value for molybdenum, making these grid panels some of the strongest carbon-carbon material ever made. Dished 30-cm carbon-carbon panels and a carbon-carbon mount ring were fabricated for a grid set retrofittable to the 30-cm NSTAR engine.

INTRODUCTION

Grid erosion is one of the remaining major life limiting phenomena for operational ion thrusters. Since ion engines are low-thrust devices, long thruster operating times are required for typical mission applications such as interplanetary or earth-orbit transfer. The required thruster lifetime for the planned NASA Solar Electric Propulsion Technology Applications Readiness (NSTAR) program, for example, is 8000 hrs. Significant grid erosion may be expected over these projected operating times^{1,2}. In order to insure that lifetime requirements are met, measures such as throttling the ion engine to lower power and thrust values and resorting to thicker molybdenum grids may have been taken, at the expense of performance of the propulsion system,

Both, reduced service life capability or engine derating to offset engine lifetime limitations, may demand the installation of additional engines on the spacecraft to meet mission requirements. Together with structural supports, gimbal mounts and additional feed lines and valving, the propulsion system mass will be increased. These issues are of particular importance in the National Aeronautics and Space Administration's (NASA) recent drive to accomplish smaller and cheaper missions³, such as the "New Millenium"⁴ or "Discovery"-class programs^{5,6}, where electric propulsion technology offers the promise of significant mass savings due to decreased propellant consumption⁵⁻⁸, provided propulsion system dry mass can be kept low.

One new technology which has the potential to significantly improve current NSTAR technology, is the use of carbon-carbon composite grids⁹⁻¹⁵. Carbon-carbon composite

material was first suggested for the fabrication of ion engine grids in 1992 by Garner and Brophy¹¹. Carbon-carbon composites consist of **graphitic** fiber in a carbonaceous matrix, consisting in part of a **graphitic** phase and a glassy carbon phase. Due to the **graphitic** nature of the composite material, carbon-carbon exhibits low sputter erosion rates, however, is considerably more rigid than graphite. Previous tests have shown that carbon-carbon has significantly lower erosion rates than molybdenum, which is the current state-of-the-art material for ion engine grid fabrication. Using the depths of erosion depressions in both carbon-carbon and molybdenum grids after a 420 **hr** wear test performed at the Boeing Defense & Space Group, Meserole¹² determined wear rates on the order of 15:1 for molybdenum vs. carbon-carbon at 300 **eV** xenon ion energies. During more recent tests, Blandino et al.¹⁶ obtained ratios of 7.3:1 and 7.7:1 for molybdenum vs. carbon-carbon wear rates at xenon ion energies of 500 **eV** and 750 **eV**, respectively. These data were obtained inside an ultra-high vacuum facility at facility pressures of 10⁻⁹ to 10⁻¹⁰ Torr, with the sample being baked out every night. Significantly longer grid lifetimes corresponding to the wear ratios given above can be expected for carbon-carbon grids than are obtainable with molybdenum grids.

In addition, carbon-carbon offers a unique characteristic with respect to its coefficient of thermal expansion (**CTE**) in a temperature range of roughly 200-800 K. At these temperatures, the **CTE** for carbon-carbon is close to zero and **negative**¹¹. Since this temperature range covers typical grid operating temperatures, carbon-carbon grids can be expected to contract slightly during thruster operation, resulting in additional stiffening of the grids. Thus, problems related to thermal warpage of the grids are avoided. Dishing of small carbon-carbon grids (e.g. 15 cm dia.) is therefore not necessary. Thin, larger diameter **carbon-carbon** grids (e.g. 30 cm dia.) may **still** require a dished grid shape due to larger deflections expected to be caused by structural launch loads or electrostatic stress between grids.

This paper summarizes ongoing research activities that have taken place at JPL in the development of carbon-carbon composite grids over the past year. The paper is structured into two parts. In Part I, results obtained from a **700-hr** carbon-carbon grid endurance test will be discussed, providing evidence of the remarkable long-life capabilities of these grids. Also, data obtained from grid **perveance** measurements at various grid gap settings will be presented as well. In Part II, results obtained in the manufacture of advanced carbon-carbon grid materials will be discussed. Activities in that area have lead to the successful fabrication of **carbon-carbon** material with a fiber volume of 57%, making it the stiffest carbon-carbon material fabricated to date.

STATUS OF CARBON-CARBON GRID RESEARCH

At JPL, three different "generations " of carbon-carbon grid panels have been developed and tested so far. The first generation of grid panels consisted of a "square weave" or "plane weave" pattern¹¹ made from Amoco P-100 fiber and **phenolic** resin. These panels were used to study material properties of carbon-carbon samples, such as **CTE**, erosion rates and structural properties¹¹, and were also used to investigate various grid hole fabrication techniques^{10,11}. In this type of lay-up, fiber bundles are woven over and under each other at **90°** angles. Initial erosion tests performed with these samples at ion energies of 28 **eV** showed surprisingly high rates of erosion for carbon-carbon - a mere 25 % smaller than for molybdenum. The corresponding samples, in the shape of **small** badges, had been placed inside the discharge chamber of a 30-cm ion engine. An important conclusion of these tests was that effects of facility gases, such as oxygen, hydrogen or nitrogen that may have been backstreaming from the test chamber into the ion engine discharge chamber, could not be

excluded¹. The presence of those gases might have affected the erosion test results, as oxygen is known to increase carbon erosion, while nitrogen is capable of lowering the erosion of molybdenum due to the formation of surface reactions¹.

Measurements of the **CTE** coefficient for carbon-carbon were also performed using this first generation of samples and showed that the **CTE** for carbon-carbon can be made very small and negative. In those tests, the CTE was measured over a temperature range from 200 to 800 K, reaching values as small as -1×10^{-6} to -2×10^{-6} 1/K. Three-point bend tests performed with these same panels revealed a **flexural** modulus of 1.6×10^{11} Pa, or about half the value for molybdenum (3.2×10^{11} Pa). The **flexural** modulus is an important grid property since it gives an indication of how far a grid may bend due to electrostatic stresses or vibrational loads imposed during launch of the spacecraft. The higher the **flexural** modulus, the more rigid the grid panel is, thus resisting electrostatic and vibrational loads better. This relatively low **flexural** modulus found for the first generation of carbon-carbon grid panels therefore required the development of more advanced lay-ups, leading to the fabrication of a "second generation" of panels.

This next grid panel type consisted of a lay-up made from unidirectional tape in a [0o/+60o/-60o]s fiber **orientation**^{9,15}. This particular lay-up was chosen because it would allow a portion of the fibers in each ply to run between the grid holes without being cut, thus increasing grid strength. The screen grid panels consisted of 6 plies, with each ply having its own, unidirectional fiber orientation. Accelerator and decelerator grid panels were manufactured by laminating two screen lay-ups back to back, forming a symmetrical lay-up. Screen grid thicknesses were 0.5 mm and accelerator and decelerator thicknesses were 0.94 mm. The unidirectional tape for these panels was fabricated at JPL and was made from DuPont E55 fiber and **phenolic** resin. Care was taken that the panel lay-up was symmetrical with respect to the center plane of the stack of plies. As was pointed out in Ref. 9, since thermal properties of the fiber and matrix material are not identical and fiber direction varies from ply to ply, temperature changes may cause the lay-up to warp the lay-up is **asymmetrical**^{9,17}.

The second **generation** panels showed an improved **flexural** modulus for the screen grid panels of 2.1×10^{11} Pa, no improvements with respect to **flexural moduli** for the accelerator and decelerator grid panels, however, were found. The second generation panels was used to assemble JPL's first operational carbon-carbon grid set⁹. Grid fabrication, however, required the exploration of a variety of hole manufacturing **techniques**⁹⁻¹¹. In particular for the high open area fraction screen grids, it was noted that the thin webbing material would break away during conventional drilling. Surface delamination at the exit side of the **drill** and the fact that fibers might get caught in the **drill** and be pulled out of the surrounding matrix material could lead to the destruction of the grid webbing. Electric discharge machining (**EDM**), ultrasonic impact grinding, laser drilling, waterjet etching and sandblasting have been explored, with EDM and ultrasonic impact grinding showing the most promising **results**⁹⁻¹¹. Screen grids were thus machined using the EDM process, while the lower open area fraction accelerator and decelerator grids could be manufactured using the much cheaper mechanical drilling **approach**⁹.

Measurements were undertaken with these grid sets to determine **perveance** and electron **backstreaming** characteristics. Similar measurements were made at the Boeing Defense & Space Group by Hedges and **Meserole**, using a square weave panel **lay-up**^{9,13}. The particular type of carbon-carbon grids used in both the Boeing and JPL tests showed lower **perveances** than those obtained with molybdenum grids at comparable open area fraction and grid **gap**^{9,13}. Possible explanations are that the molybdenum accelerator and decelerator grids were thinner than the corresponding carbon-carbon grids (0.38 mm vs. 0.94 mm in the JPL tests) and that

the grid gap for molybdenum grids could narrow as the grids heat up and expand. Thus, the **perveance** limit for the molybdenum grid was reduced to about 1000 V at 500 mA beam current versus about 1300 V for the carbon-carbon grid set at the same beam current in the JPL tests.

Since the **perveance** of a grid is an important performance parameter that indicates how much current can be extracted from an ion engine at a given voltage and grid gap, maximizing this parameter is desirable in order to obtain higher thrust densities. Currently, advanced carbon-carbon grids of a “third generation” are in the process of fabrication, with the panel fabrication complete at this point. These panels are thinner than the previous ones (0.4 mm) and have a higher fiber volume (about 57 %), resulting in the strongest carbon-carbon material ever made. **Flexural moduli** approaching the value for molybdenum (3.45×10^{11} Pa) have been obtained. Fabrication of these advanced grid panels will be discussed at the end of this paper.

An interesting activity currently being undertaken at JPL is the development of carbon-carbon grids having non-circular grid apertures, in the form of elongated holes or slots, which have recently been proposed by the authors¹⁸⁻²⁰. The slotted carbon-carbon grids are the present day analog to the historical wire-grids investigated by Kaufmann in the 1960's²¹. Whereas wire-grids suffered from problems due to thermal distortions of the wires, slotted carbon-carbon grids circumvent this difficulty because of their negative CTE. When heating up during operation, the carbon-carbon material contracts, actually increasing the stiffness of the grid. Slotted carbon-carbon grids are presently in the process of being tested at JPL and development work in this area will be described in a companion paper¹⁸.

In the following sections, current activities in the area of carbon-carbon grid research, such as a 700-hr carbon-carbon grid wear test, carbon-carbon grid **perveance** experiments at varying grid gaps and, finally, advanced grid panel fabrication will be described.

PART I: CARBON-CARBON GRID TESTING

Description of Test Hardware

Carbon-Carbon Grid Sets

A detailed design description of the grid sets used in the endurance test has previously been given in Reference 9. These grids have previously been used in tests described in that reference. Briefly, the grid sets consist of three grids, the screen, accelerator and negatively biased decelerator grid (SAND-optics) and are mounted to a graphite (G540 grade, Tokai Carbon Co.) mount ring via **Steatite (MgO·SiO₂)** ceramic spacers. A photograph of an assembled carbon-carbon grid set is shown in Fig. 1. The grid panels used are of the previously described second generation, i.e. made from unidirectional tape in a $[0^\circ/+60^\circ/-60^\circ]_s$ lay-up. Overall grid diameter is 19.4 cm, with the beam area being 15 cm in diameter. Each grid features 4268 holes spaced 2.21 mm apart.

Two grid sets were used and run simultaneously during the tests, mounted on two segments of JPL's segmented ion engine. Following the notation used in Reference 9, these grid sets will be referred to as grid set A and C, respectively, named after the ion engine segments they were originally mounted to⁹. Screen grid aperture diameters are 1.86-1.93 mm, aperture diameters for the accelerator and decelerator grids are 1.18 mm and 1.7-1.72 mm, respectively. This leaves webbing thicknesses between the grid apertures of roughly 0.3 mm, 1 mm and 0.5 mm, respectively, for the screen, accelerator and decelerator grids. The

resulting open area fractions are then found to be on the order of 64- 69%, 25- 26% and 54- 55%, respectively.

Grid gaps were varied for the **perveance** tests between 0.64 mm and 0.51 mm between screen and accelerator grids. Accelerator-decelerator grid gaps were held constant at 0.25 mm. For the endurance test, grid gaps between the screen and accelerator grids were 0.74 mm for set A and 0.64 mm for set C. Grid gaps between the accelerator and decelerator grids were set at 0.25 mm for both grid sets. The grid gaps are maintained by mounting each grid to a set of six of the **previousl**y mentioned **Steatite** spacers, each set having a different height. The detailed grid properties of the two sets A and C are listed in Table 1. Overall grid set mass, including mount ring, is roughly 220 grams, varying by about 3 grams between the different sets. Grid gaps settings listed in Table 1 are those used for the endurance test. Grid aperture values, grid thicknesses and masses are all **pre-endurance** test data.

Segmented Ion Engine

As mentioned, testing of the carbon-carbon grid sets for both the **perveance** as well as the endurance experiment was performed with the grids mounted to two segments of JPL's segmented ion thruster (SIT). The assembled SIT thruster is shown in Figure 2. A detailed description of this engine type has been given in Reference 22. Briefly, the SIT engine divides a large ion engine into four smaller, equally sized segments. Each segment is equipped with a separate discharge and keeper power supply, however, all for segments are run from a single set of high-voltage screen, accelerator and decelerator supplies. Propellant flows to each segment (main and cathode) can be controlled individually. However, the SIT thruster is only equipped with one central neutralizer, visible in the center of the assembly in Fig. 2. Engine neutralizer and cathode designs are identical and described in Reference 23.

The thruster bodies of the different segments are manufactured from spun 6061 aluminum and are identical. Two rings of **somarium-cobalt** magnets, one located at the upstream end of the semi-conical discharge chamber and one at the downstream end, close to the grid interface, generate the magnetic field. The four segments are mounted to an aluminum base plate and surrounded by a screen, held at ground potential.

The purpose of the SIT design was to provide a long-life alternative to existing 30-cm ion engine hardware for interplanetary missions. By turning off power to individual segments of the SIT-thruster, gross throttling of the engine can be realized to account for reduced solar power availability as the electric spacecraft travels outward away from the sun. At the same time, those segments that are currently unused, are no longer subject to wear-out and can be saved for later in the mission,

However, when searching for a suitable engine to perform the carbon-carbon grid tests, it was found that the SIT thruster is also an ideal test bed for the development of advanced grid technologies. First, since the SIT thruster allows for simultaneous testing of several grid sets, testing for multiple sets can be accomplished faster. Second, since simultaneous testing of several grid sets will reduce facility occupation and allow the test operator to conduct several grid tests at the same time, using the SIT thruster for testing advanced grid technologies is cheaper. Cost are also saved due to the fact that each segment of the SIT thruster only requires a 15-cm grid design. Fifteen centimeter grid sets are cheaper to fabricate than 30-cm sets, for example. Third, and finally, by testing several grid sets of the same kind, a larger statistical sample of data can be obtained in one test run for a particular grid design, or, if different grid designs are tested simultaneously, all grid sets are tested under the same conditions, resulting in a better test environment.

Table 1: Description of Grid Sets

Segmented Ion Engine Grid Sets (Endurance Test Settings)		
Component	Grid Set A	Grid Set C
Grid Material	Carbon-Carbon	Carbon-Carbon
Grid Shape	Flat	Flat
Grid Diameter (cm)	19.4	19.4
Beam Diameter (cm)	15	15
Hole Quantity	4268	4268
Hole Spacing (mm)	2.21	2.21
Screen Grid		
Thickness (mm)	0.52 (+0.01/-0.04)	0.56 (+/- 0)
Hole Dia. (mm)	1.86(+/- 0.06)	1.93(+0.01/-0.003)
Open Area Fraction	0.64	0.69
Weight (gram)	14.1	16.4
Manufacturing Technique	EDM	EDM
Accelerator Grid		
Thickness (mm)	0.94 (+/- 0)	0.94 (+/-0)
Hole Dia. (mm)	1.18 (+/- 0)	1.15 (+/-0.01)
Open Area Fraction	0.26	0.25
Weight (gram)	42.5	42.9
Manufacturing Technique	Mechanical	Mechanical
Decelerator Grid		
Thickness (mm)	0.94(+0.02/-0.004)	0.94 (+/- 0)
Hole Dia. (mm)	1.7(+/-0.03)	1.72(+/- 0.004)
Open Area Fraction	0.54	0.55
Weight (gram)	31.6	31.3
Manufacturing Technique	Mechanical	Mechanical
Screen-Accel Gap (mm)	0.64	0.64
Accel-Decel Gap (mm)	0.25	0.25
Mount Ring		
Material	G540 Graphite	G540 Graphite
Weight	67.7	67.9
Manufacturing Technique	Mechanical	Mechanical
Spacers	Steatite	Steatite

Perveance Tests

Test Procedures

The **perveance** of an ion engine grid describes its ability to extract current from the discharge chamber at a given grid voltage. The beam current is restricted due to space-charge limitations (Child-Langmuir law) and determined by the geometry of the grid (thickness, grid aperture diameter and grid separation). Here, **perveance** measurements were performed by keeping the screen current constant while varying the total grid voltage between the screen and accelerator grid and measuring the accelerator and decelerator impingement currents. In order to ensure a constant screen current, the discharge current had to be adjusted accordingly. The screen current is slightly larger than the beam current by an amount equal to the sum of accelerator and decelerator impingement current due to the particular arrangement of screen, accelerator and decelerator power supplies in the engine circuit,

Results

Results obtained for the **perveance** tests are shown in Figures 3 through 5. Figures 3 and 4 depict the accelerator impingement current as a function of total voltage between screen and accelerator grid for two different screen-accelerator grid gap settings for grid set C. The accelerator-decelerator gap is identical in both cases, being 0.25 mm (0.01 O"). In Fig. 3, the screen-accelerator grid gap is 0.51 mm (0.020"), whereas in Fig. 4 this gap is set at 0.64 mm (0.025"). As can be seen, **perveance** of the grid set is improved by closing the screen-accelerator grid gap, as expected. When comparing these data with **perveance** data obtained earlier for a 15-cm molybdenum grid set gapped at 0.51 mm between screen and accelerator grid23 (Fig, 5), it can be noted that for a beam current of 500 mA the accelerator impingement current begins to increase below 1100 V for the molybdenum grid, with the "knee" of the curve located close to 1000 V. For the carbon-carbon grids used here, the accelerator grid impingement current begins to raise below 1200 V, with the "knee" of the curve located around 1100V_o.

Several explanations can be found to account for the higher **perveance** of molybdenum grids. First, due to the larger thickness of the carbon-carbon accelerator grid of 0.94 mm versus only 0.38 mm for the molybdenum grid, the thicker carbon-carbon accelerator grid is capable of intercepting more beam ions than the thinner molybdenum grid, resulting in a higher direct grid impingement current. Secondly, grid gaps may shrink for molybdenum grids as these grids warm up and expand. A smaller grid gap will result in a larger grid **perveance**. However, the differences between the carbon-carbon and molybdenum grids are relatively small and, using thinner carbon-carbon grids, are expected to disappear. Thinner carbon-carbon grids are currently in fabrication and will be discussed later,

700-hr Endurance Test

Test Set-up and Scope of the Test

Two previously used carbon-carbon grid sets, set A and C of Reference 9 described in Table 1, were subjected to a 700-hr wear test. The grid sets are shown mounted to two segments of the segmented ion engine in Fig. 6. As can be seen from the photograph in Fig.6, the carbon-carbon grids are coated with a layer of metallic deposits, giving the grids a shiny surface finish, rather than the deep black appearance of carbon-carbon. A photograph of this layer, when observed under an electron microscope, is shown in Fig. 7. This picture was taken after the endurance test at the boundary of one of the erosion "grooves" shown in Fig. 8. This picture was taken at the center location of the downstream side of the decelerator grid of grid

set C, The “groove” formation shown is typical during grid erosion and consists of relatively **uneroded** layers surrounding the grid holes and areas of significant erosion in the “grooves” between the holes. These erosion patterns will be discussed in greater detail below.

Electron microscope scans along the boundary of the **uneroded** and eroded areas revealed that this layer of metallic deposits was around $6\text{ }\mu\text{m}$ thick at its thickest locations, determined from measurements from the photograph. An x-ray fluorescence scan performed at this location revealed that the small metal hillocks in Fig. 7, forming the “rocky” portion of the deposit, were mostly composed of molybdenum, while the darker, flatter regions of deposits were mostly tantalum, with heavy traces of molybdenum. The x-ray spectrum obtained from this scan is shown in Fig. 9. The lighter trace shows the spectrum obtained from the molybdenum hillocks, while the darker trace was measured in the flatter tantalum “mare”. Given the major constituents of this deposition, it was concluded that this contamination resulted from **backspattered** material from a Faraday-probe rake that was moved through the ion beam during an earlier **experiment**²⁴. Although it would have been preferred to use new, previously unused and clean carbon-carbon grid sets for this test, new carbon-carbon grid panels had not been available at the start of the wear test.

Given the layer of metal deposits on the carbon-carbon grids, some considerations regarding the validity and scope of this wear test are in order. Previous tests have shown that complete penetration of a 0.38 mm molybdenum grid occurred after less than 145 hours at similar **backpressures** in “pit” locations centrally located between three adjacent grid apertures (Fig. 10)². These tests had been performed at an ion impingement energy of 500 eV, using krypton as a propellant. Sputter yields for krypton and xenon, which was used in the **carbon-carbon** test described here, on molybdenum are very **similar**¹. If one were to assume a constant wear rate for the entire duration of the test (which is by no means proven and merely a simplifying assumption) a $6\text{ }\mu\text{m}$ thick molybdenum layer would have been eroded away at those locations in about 20 minutes. Here, a value of about one hour is assumed instead to account for uncertainties in the estimate. Taking into account that the wear rate of molybdenum is lower at 100 eV ion impingement energies (which were the energy levels encountered for decelerator ion impingement during this test) than at 500 eV by a factor of 15 (see Reference 25), a $6\text{ }\mu\text{m}$ molybdenum layer would have been completely eroded at the described “pit” locations within 15 hours, exposing the underlying carbon-carbon for the remainder of the test.

The layer coating the carbon-carbon grids not only contained molybdenum, but also heavy traces of tantalum. According to Reference 25, the wear rate for tantalum is only slightly lower than that for molybdenum. At 100 eV, the factor by which tantalum erosion rates are lower than molybdenum rates is 0.96. Thus, a $6\text{ }\mu\text{m}$ thick tantalum layer would have completely eroded through at the “pit” locations within less than 15.5 hours under those simplifying assumptions. It should be noted, however, that from Fig. 7 the tantalum “mare” appears flatter and thinner than the “rocky” molybdenum deposits. If the composition of the deposited layer visible in Fig. 7 was similar in the areas that have been eroded, it should have taken less time to erode the thinner tantalum layer. In any case, it is safe to conclude from these estimates that carbon-carbon material was exposed for the largest portion of the test duration, probably well in excess of 600 hours.

It is understood that this wear test should be repeated once new carbon-carbon grid sets become available, followed by detailed **profilometer** studies. Ideally a 15-cm molybdenum grid should be mounted to one of the other engine segments for comparison. Due to the presence of the metal coating no **profilometer** scans were attempted here and unfortunately no molybdenum grid set was available for this test,

Test Conditions and Procedure

Engine test conditions for the endurance test are shown in Table 2. The beam current per segment was maintained at values just between 500 and 550 **mA** for segment A and between 400 and 550 **mA** for segment C. Screen grid voltage was set at 1200 to 1250 V, and accelerator voltage at 100 V except for the first 60 hours where a higher value of 120 to 140 V had been chosen. Decelerator voltage was set between 75 and 100 V. Discharge current was around **4 A** per segment and discharge voltage was maintained between values of 24 and **30 V**. Main flow rates were around 7 seem and cathode flow rates around 1 seem per segment. The thruster beam currents, screen, accelerator and decelerator voltages, and accelerator and decelerator impingement currents are plotted in Fig, 11 through 15 versus time for the duration of the test. As Fig, 15 shows, accelerator and decelerator grid currents varied between 2 to 5 **mA** in the case of segment A. The recycle rate (arcing between grids) is shown in Fig. 16. As can be seen from this plot, it rarely exceeded 3 **arcs/hr** and for extensive portions of the test stayed below 1 **arc/hr**. The vacuum tank pressure was maintained at a fairly high **level** of around 4×10^{-5} **Torr**. The test was conducted in a 2.4 m diameter and 5 m long, diffusion pumped vacuum facility, using one 0.81 -m and one 1.2 m diameter **oil** diffusion pump.

The test results were evaluated by means of visual inspections under an electron microscope before and after the test. X-ray fluorescence spectroscopy was performed on the grids after conclusion of the test to analyze various surface features visible in the electron microscope scans. The grids were weighed before and after the test to determine any mass loss from the grids due to erosion, Grid thicknesses were measured in order to obtain a crude estimate as to whether mass loss measurements would correlate with an overall thinning of the grid. Finally, grid apertures were measured after the test at various locations on the grid and compared with pre-test conditions to determine the degree grid hole erosion.

Table 2: Nominal Thruster Operating Parameters for Endurance Test

Parameter	Segment A	Segment C
Beam Current (mA)	520-550	460-540
Screen Grid Voltage (V)	1250	1250
Accelerator Grid Voltage (v)	100	100
Decelerator Grid Voltage (v)	75-100	75-100
Accelerator Grid Current (mA)	4-7	3.5-4.5
Decelerator Grid Current (mA)	4	3.6
Discharge Current (A)	4	4
Discharge Voltage (V)	28	24-30
Main Flow Rate (seem)	7	7
Cathode Flow Rate (seem)	1-1.5	1-1.5
Tank Pressure (Air) (Torr)	4.5×10^{-5}	4.5×10^{-5}

Visual Inspection and X-Ray Fluorescence

Pre-Test Conditions

Both, grid sets A and C were visually inspected before and after the test. Results were similar for both grid sets, so that here only features found for grid set C will be discussed. Figures 17 through 19 show the pretest conditions of the decelerator, accelerator and screen grids of set C at the downstream sides of the grids close to the grid center. Photographs were also taken on the respective upstream sides and at half-radius and full-radius positions of the grids for both sides and both grid sets. However, surface features are fairly similar at all those locations so that here only Fig. 17 through 19 are shown.

As can be seen from Fig. 17 through 19, no erosion patterns were visible on the carbon-carbon grids despite the fact that the grids had been in use for 108 hours prior to the wear test for various proof-of-concept testing⁹ and plume measurement experiments²⁴. All photographs also show surface “striations”, revealing the fiber directions of the outer surface ply. In particular in Fig. 17, showing the downstream side of the center region of the decelerator grid of segment C, the fact that fibers can clearly be identified indicates that the metallic surface deposits discussed earlier are thin. As mentioned, grid appearances are virtually identical to those shown in Figures 17 through 19 at other locations of the grids and for grid set A.

Decelerator Grid - Post -Test Inspection

After 700 hours of testing under the conditions given above, erosion patterns formed on the downstream side of the decelerator grid, as shown earlier in Fig. 8. Figures 20 and 21 show the condition of decelerator grid C at the downstream side at mid- and full-radius positions. As can be seen, typical erosion “groove” formations are visible at the mid-radius position, none, however, are visible at the edge of the active beam area. As was noted earlier, and shown in Figure 7, the difference between the lightly colored regions in Figures 8 and 21 and the dark erosion grooves is a deposited layer of metal, mostly molybdenum and tantalum, that had coated the decelerator grids before initiation of the endurance test. This layer was likely formed from **backsputtered** material eroded off a probe rake that was used to conduct **Faraday**-probe measurements in the plume of the segmented ion engine²⁴. The darker regions show the underlying carbon-carbon surface, while the lighter regions around the grid apertures bear a surface of mostly **uneroded** metal deposits. A closer inspection of those areas shown in Figures 22 through 27 reveals further details. Figure 22 shows a region close to the center of the downstream side of the **decel** grid. Apart from the overall erosion pattern, it can be noted that at those webbing locations where the fiber direction is normal to the grid hole edges, surface delamination has occurred. Some of those surface delamination regions at center and midway locations on the grid are shown close-up in Figures 23 through 25. Figure 24 shows a portion of the surface material at that webbing location in the process of delamination.

It seems obvious that the described webbing locations are prone to delamination, since they correspond to those areas where the fiber segments are the shortest, thus providing little opportunity for the short segments to build up sufficient **interlaminar** strength between themselves and fiber layers underneath. However, close inspection of Figures 22 through 25 reveals that the underlying areas, now exposed to the surface after delamination of the top layer, also show the same surface coating as the **uneroded** areas. This seems to indicate that surface delamination did occur at those locations either very early during the endurance test, allowing for redeposition of the metal layer in the delaminated areas of the webbing, or before initiation of the test, possibly even during the fabrication process. The **decel** grid was mechanically drilled and drill bits are known to cause surface delamination at the exit side of the drill⁹. An inspection of some of the decelerator grids performed during a previous study⁹ did

not reveal any extensive surface delamination of this kind, however, it is possibly that the exact locations shown in Fig. 22 through 25 were not scanned previously.

Studying Fig. 26 and 27, however, indicates that, first, surface delamination is not restricted to the previously described areas of the webbing material where fibers are oriented normal to the grid hole edges and, second, shows cases of surface delamination that definitely have occurred during the endurance test, since the metal coating has been removed together with the delaminated carbon-carbon material. As was already evident from Figures 22 through 25, and shown in greater detail in Figures 26 and 27, only a thin upper layer of one to several fiber thicknesses has been removed in all cases inspected on the **decel** grid after 700 hours of testing. By no means has the decelerator grid been structurally compromised by this delamination process.

Probably one of the most important finds of this study, however, can be derived from a close inspection of Fig. 23 through 27. As can be seen on Fig. 23, for example, outside the delaminated areas fibers that are coated with metal deposits close to the hole edges run the entire width of the webbing, through the “groove” areas where the metal deposit has been eroded, to the opposite side of the webbing area, where the same fibers appear to be coated again with a metal layer. These fibers therefore appear to belong to the top surface layer because they are coated with the metal deposits, however, they show virtually no erosion in the exposed, darker areas. Even in areas where “pits” should form (compare with Fig. 10), such as those shown in Figures 24 and 27, no erosion pattern in the fiber material is apparent even after 700 hours of testing, demonstrating the extraordinary long-life capabilities of carbon-carbon grids.

Another surprising observation was made when inspecting the hole walls of the decelerator apertures, observed from the downstream side. As can be seen in Fig. 28, deposits have formed at the upstream end of those wall areas. An x-ray fluorescence scan of those deposits is shown in Fig. 29 and reveals that these deposits are composed mostly of redeposited carbon with substantial amounts of xenon trapped inside them. Although the fluorescence scan in Fig. 29 identifies a barium line, closer inspection of the spectrum revealed that this line is more likely to be a second xenon line. Trapping of xenon is most likely made possible by the porous character of the carbon-carbon material and its redeposited layers. In view of grid erosion it is important to note that the existence of redeposited carbon shown in Fig. 28 indicates that some carbon-carbon erosion did occur on the grids, probably in thin layers along the darker surface areas, invisible in Figures 22 through 27 or inside grid holes by direct ion impingement, discussed below.

The upstream side of the decelerator grid of segment C is shown at center, mid-radius and full-radius locations in Figures 30 through 32. When comparing center, mid-radius and full-radius surface features from Figures 30 through 32, it becomes apparent that the webbing surfaces become less “striated” with the fibers appearing more coated as one moves from the edge of the active beam area to the center. However, even close to the edge surface deposits can be noted (see Fig. 33). The surface coating was analyzed by means of x-ray fluorescence scans and the results are shown in Fig. 34. Two spectra were taken at the webbing location shown in Fig. 33. The first trace, shown dark in Fig. 34, was taken at webbing locations shown in the upper right hand corner of Fig. 33. The lighter trace of Fig. 34 was taken at webbing locations in the left-hand lower corner of Fig. 33. As can be seen by comparing both spectra, surface deposits again consist mostly of carbon, with traces of xenon trapped in the deposits. The amount of trapped xenon is somewhat higher in the areas of the webbing material shown in the lower left corner of Fig. 33 and thus not uniform. The surface deposits also contain traces of silicon which may be due to the silicon pump oil used in the oil diffusion pumps, or due to surface treatment (grinding) of the grids during fabrication.

Figure 35 shows a close-up view of the decelerator holes as viewed from the upstream side of the grid, showing the already encountered carbon redepositions on the hole walls. As can be seen by inspection of the hole shown in the upper right corner of Fig. 35, portions of the redeposited carbon material are beginning to break loose. Measurements taken from the photograph in Figure 35 indicate that the thickness of those carbon “flakes” is on the order of 50 μm . This observed flaking of grid material is concerning, since conducting material, redeposited and then flaking off grid surfaces may lead to grid failure, in particular when those flakes are being released into the inter-grid space between two adjacent grids, potentially shorting out those **grids**². It should be noted that beginning at about 400 hours into the wear test shorting between the accelerator and decelerator grid of segment C was noted, as shown in Fig. 16, and that the shorting arcs may have been due to loosened carbon flakes as those shown in Fig. 35. However, this explanation is purely speculative at this point.

Accelerator Grid - Post-Test Inspection

Post-test photographs of the downstream side of the accelerator grid are shown in Fig. 36 through 38. Most notable are the light “halos” surrounding the accelerator grid apertures, in particular at center and mid-radius positions of the grid. X-ray fluorescence scans revealed that the “halos” represent **metal** deposits. According to Fig. 39, these deposits are composed mostly of molybdenum, containing some traces of tantalum, iron and chromium, as well as aluminum. **Pre-test** photographs (Fig. 17) show that the same type of deposits was found on the accelerator grid before initiation of the endurance test and is believed to be from the same source as the decelerator grid deposits. As can be seen from Fig. 39, a control trace taken at the darker locations between the “halos” indicates mostly carbon being present at these locations, together with traces of tantalum. The difference in composition of the “halos” and the darker carbon areas surrounding them is very distinct. It can also be noted from the spectra of Fig. 39 that the xenon peak is almost non-existent, indicating that not much xenon has been trapped on the downstream side of the accelerator grid.

Once again, after inspecting Fig. 36 through 38, the virtual absence of erosion that is so predominant in molybdenum grids after comparable run times, has to be noted. However, a close-up inspection of the upper right corner of Fig. 36, shown in Fig. 40, reveals the same kind of carbon redepositions noted earlier on the downstream side of the decelerator grid. As can be seen in Fig. 40, a portion of this carbon redeposition has flaked off. This carbon flake was on the order of 350 μm long, provided it broke off as a single piece. This flake was therefore long enough to potentially short out the accelerator and decelerator grid. Carbon redepositions can also be found located on the inside of the accelerator grid holes, shown in Fig. 37 and 38.

Inspection of the upstream side of the accelerator grid revealed ring-shaped features surrounding the accelerator grid holes, at all grid locations from the center to the edge of the grid (see Figures 41 through 43). A close-up view of one of the ring-shaped deposits around the holes is shown in Fig. 44. Apart from the ring-shaped deposit, carbon fibers are clearly visible, as on Figures 41 through 43, indicating that carbon surface deposits may be less on the upstream side of the accelerator grid than on its downstream side. An x-ray fluorescence scan performed at the ring-shaped feature (Fig. 45) indicates that this deposit is mostly made of barium, calcium, silicon and oxygen (dark trace in Fig. 45). A control scan of areas located outside the ring-shaped deposit area shows mostly carbon (off-scale) and none of the aforementioned elements (light trace of **Fig. 45**). Thus the difference in composition of the **ring-shaped** deposits and its surroundings is very distinct. Barium and oxygen may have very well been the result of cathode erosion inside the discharge chamber with eroded material then

redepositing on the upstream side in areas of the accelerator grid shaded from the direct line-of-sight of the discharge chamber by the screen grid. The distinct silicon deposits found in the ring-shaped areas may have resulted from discharge chamber erosion. The discharge chamber is made of 6061 aluminum, which contains a 0.670 trace of silicon 26. The calcium deposits may also be the result from cathode erosion.

Screen Grid - Post-Test Inspection

Figures 46 through 48 show the downstream side of the screen grid at center, mid- and full-radius positions. Again, in particular at grid center locations, a redeposited layer of carbon can be noted, shown close-up in Fig. 49. Figure 49 also shows the very thin webbing between the holes, a direct result of the high open area fraction of 69% for this grid. The screen grid upstream side is shown in Figures 50 through 52 from locations at the center to the edge of the beam area. Again, carbon fibers are clearly visible at center and mid-radius positions on the screen upstream side, indicating low carbon redeposits here. Closer to the edge, however, a layer of non-carbon deposits is clearly visible, appearing light in color in the electron microscope scan. A closer view of the contaminated area (Fig. 53) and an x-ray fluorescence scan taken at that location indicates heavy aluminum, copper, magnesium, silicon and oxygen deposits in the lighter areas of Fig. 53 (dark trace of Fig. 54). The lighter trace of Fig. 54 was measured at the darker locations of Fig. 53. Here, the deposits are mostly made of carbon, aluminum and smaller traces of copper, silicon and oxygen.

Knowing the composition of 6061 aluminum used in the fabrication of the discharge chamber to be 0.690 silicon, 0.28 % copper, 1.070 magnesium and 0.2070 zinc with the remainder being aluminum²⁶, it is relatively easy to explain most of the deposits found near the upstream edge of the screen grid. With this edge being located close to the discharge chamber wall, erosion products coming from that wall likely have deposited at this location on the grid. The strong spectral line of oxygen, however, cannot be explained, in particular in view of the absence of a barium line, which could one have lead to conclude that redeposited cathode erosion products were responsible for this part of the x-ray spectrum,

Grid Aperture Measurements

Table 3: Pre-and Post Test Grid Aperture Diameters for Grid Set A (Dimensions in mm)

Grid	Pre-Test		Post-Test					
			Center		0.5 R		R	
Screen	1.8		1.888	+0.002/-0.013	1.895	+0.007/-0.005	1.881	+0.004/-0.004
Accelerator	1.18		1.179	+0.028/-0.029	1.196	+0.011/-0.012	1.198	+0.052/-0.030
Decelerator	1.699	+0.025/-0.033	1.710	+0.005/-0.006	1.685	+0.002/-0.001	1.688	+0.006/-0.009

Table 4: Pre-and Post Test Grid Aperture Diameters for Grid Set C (Dimensions in mm)

Grid	Pre-Test				Post-Test			
	Center				0.5 R		R	
Screen	1.929	+0.007/-0.003	1.950	+0.001/-0.002	1.925	+0.005/-0.007	1.901	+0.009/-0.009
Accelerator	1.147	+0.003/-0.003	1.182	+0.009/-0.006	1.150	+0.003/-0.002	1.143	+0.013/-0.018
Decelerator	1.716	+0.004/-0.004	1.718	+0.009/-0.007	1.752	+0.008/-0.007	1.783	+0.025/-0.018

Pre-and post test grid aperture measurements are shown in Tables 3 and 4 for grid sets A and C, respectively. Both **pre-** and post-test measurements were performed with a Kodak Contour optical comparator, Model 14-5. Usually, three to four different holes were measured at the center, mid- and full radius positions. The results were averaged and the largest deviations from the mean were noted in the tables. For the **pre-test** conditions, only one set of hole measurements is given, taken close to the center of the grid.

As can be seen from Tables 3 and 4, a slight increase in hole diameter for the accelerator grid holes can be noted. For grid set A, the hole diameter close to the center of the grid varied between 1.207 mm, representing a maximum hole diameter increase of about 0.06 mm, and 1.15 mm. This large scatter may be attributed to the fact that some holes have been widened by erosion while others have been narrowed due to carbon redeposition on its wall surfaces. The latter kind of holes was characterized by rather irregular hole shapes due to direct ion impingement. Similar variations in hole size can be found near the edges of the accelerator grid A, with the largest increase in hole diameter being 0.07 mm.

Accelerator grid hole diameters for grid set C show less scatter near the center and **mid-**radius positions but larger scatter near the edges of the grid where carbon-redeposits were found (Figures 38 and 43). As can be noted from Figures 36 and 41, carbon deposits on hole walls near the center of the grid were minor, thus a fairly constant hole size was measured. Table 4 shows that accelerator hole diameters have increased by about 0.035 to 0.045 mm near the center of the grid, but stayed almost constant at mid-radius positions and near the edge of the beam area.

Decelerator grid hole diameters for grid set A have increased near the center of the grid by an average of 0.010 mm, however, have hardly changed at **all** or even narrowed near the edges of the grid which maybe attributed to carbon deposits on the wall surfaces of the hole. In the case of grid set C, decelerator grid holes appeared to have remained almost unchanged near the grid center, where the current density is the highest, yet seem to have widened at **mid-**radius positions and near the grid edge, probably due to direct ion impingement. Evidence for direct ion impingement can be seen in Fig. 21, showing decelerator grid holes near the edge of the grid, **eroded** into elliptical and "tear drop" shapes. Screen grid holes have widened for grid set A at all grid locations, however, only at center positions for set C. The average hole diameter increase close to the grid center is 0.088 mm for the screen grid of set A and 0.020 mm for the screen grid of set C,

In summary, hole sizes seem to have increased for both grid sets on **all** grids to some degree at various locations on the grids. However, the grid locations of largest hole diameter increase vary from grid to grid and are not always the center locations as one might expect. Misalignment of the outer holes might have **led** to direct ion impingement and caused erosion here. Measurement errors using the particular Kodak optical comparator have been determined to be less than 0.003 mm by repeatedly measuring the same hole and recording differences between the individual measurements.

Grid Thickness Measurements

Table 5: Thickness Measurements for Grid Set A (all dimensions in mm)

Component	Pre-Test	Post-Test
Screen Grid		
Center	0.518 +0.005/-0.084	0.511 +0.010/-0.008
Mid-Radius	0.506 +0.053/-0.084	0.518 +0.028/-0.032

Edge	0.531 +0.028/-0.023	0.518 +0.019/-0.018
Accelerator Grid		
Center	0.973 +/- 0.001	0.975 +/- 0.001
Mid-Radius	0.972 +0.002/-0.005	0.973 +/- 0.005
Edge	0.964 +0.025/-0.018	0.956 + 0.013/-0.018
Decelerator Grid		
Center	0.970 +0.004/-0.006	0.955 +/-0.012
Mid-Radius	0.982 +0.034/-0.010	0.978 +0.007/-0.008
Edge	0.956 +0.004/-0.010	0.950 +/- 0.012

Table 6: Thickness Measurements for Grid Set C (all dimensions in mm)

Component	Pre-Test	Post-Test
Screen Grid		
Center	0.584	0.576 +0.003/-0.004
Mid-Radius	0.582 +0.002/-0.008	0.577 +0.003/-0.005
Edge	0.576 +0.001/-0.002	0.564 +0.004/-0.007
Accelerator Grid		
Center	0.969	0.968 +/-0.006
Mid-Radius	0.972 +0.002/-0.003	0.968 +/-0.003
Edge	0.965 +/- 0.003	0.959 +0.007/-0.009
Decelerator Grid		
Center	0.961 +/- 0.004	0.959 +/-0.006
Mid-Radius	0.956+0.010/-0.016	0.958 +0.011/-0.008
Edge	0.955 +0.010/-0.009	0.957 +0.004/-0.007

have recorded the major or minor axis or values inbetween rather than the diameter of a truly round hole. Furthermore, using the optical comparator, hole sizes are measured from the projected shadow of a section of the grid on a large screen. Carbon deposits, unless extensive, are not always clearly detectable from the shadow image of the grid and may thus have led to the measurement of smaller hole diameters than were measured at the beginning of the test.

Grid thicknesses were measured before and after the endurance test with a micrometer. Measurements were taken at the edge of the grids (close to the mounting holes outside the active beam area), at mid-radius positions and close to the center of the grids. For each radial position six roughly equidistant locations were chosen for the measurements along the periphery. The grids were marked before the endurance tests and post-test measurements were taken at roughly the same locations as pre-test measurements. The values obtained for each radial position were averaged and the largest deviations from this mean were recorded and are listed together with the average value in Tables 5 and 6. The micrometer was equipped with a digital readout and was capable of indicating values with a 0.00005" (0.001 mm) resolution. However, repeated measurements performed at certain selected locations on the grids yielded a repeatability of about 0.0001" to 0.0002" (0.003 mm to 0.005 mm).

Upon inspection of the values listed in Tables 5 and 6, it has to be concluded that any differences noted between the grid thicknesses in pre- and post-test conditions are well within the margin of error, both the measurement error for the micrometer as well as the deviations noted in grid thicknesses for a given radial position.

Grid Mass Loss Measurements

Table 7: Grid Masses of Grid Sets A and C (All Masses in gm)

Component	6/14/94	11/23/94 (Pre-Test)	3130/95 (Post-Test)	700-hr Tests Δ
Grid Set A				
Screen	14.1	14.03	14.075	+0.045
Accelerator	42.5	42.49	42.222	-0.268
Decelerator	31.6	31.71	31.628	-0.082
Total	222.4	223.49		
Grid Set C				
Screen	16.4	16.36	16.395	+0.035
Accelerator	42.9	42.90	42.638	-0.262
Decelerator	31.3	31.40	31.350	-0.050

Grid mass loss measurements were performed at three points in time during the evaluation of the second generation carbon-carbon grids. The first set of measurements, shown in the first column of Table 7, was performed before installing the grids onto the engine and before any tests had been conducted. The second set of data, shown in the second column of Table 7, show grid masses as measured before the endurance test was initiated but after 166 hours of operation for grid set A and 108 hours for grid set C to conduct proof-of-concept type testing⁹ and plume measurements²⁴. As can be seen by inspecting the decelerator grid masses closely, these masses actually increased during this first series of tests, which is being attributed to the metal coating found in particular on the decelerator grids, resulting from backspattered material that was eroded from a Faraday-probe rake during the plume measurements²⁴. The increase in mass for both decelerator grids A and C is on the order of 0.1 gm.

Given the rough thickness measurement of the metal coating from Fig. 7, a simplified analysis may be performed to determine whether the measured mass increase is consistent with the observed thickness of the coating. Assuming for the moment that the metal layer was distributed uniformly over the active 15-cm diameter grid area with an open area fraction of 0.55 for the decelerator grid, the surface area occupied by the coating is determined to 80 cm². The tallest surface features of the deposited metal layer were estimated at 6 μ m. The average value for the thickness of the coating is certainly less, however, is difficult to estimate. If one were to use the value of maximum thickness for the average coating thickness to obtain an upper bound for the deposited mass, the volume occupied by the metal coating is calculated to 0.05 cm³. Molybdenum and tantalum densities are 10.2 gm/cm³ and 16.6 gm/cm³, respectively. The exact ratios for the two metals present in the coating is unknown. If the layer were composed of equal amounts of molybdenum and tantalum, the total mass of the layer can be estimated to 0.65 gm. This calculated value is within less than an order of magnitude of the measured value. However, given the rather arbitrary assumptions regarding the composition of the layer and its average thickness nothing more than rough, first order mass estimate is to be expected.

The third column finally shows the post-endurance test masses measured. Both, accelerator and decelerator grids lost mass. Decelerator mass losses were on the order of 0.05 to 0.08 gm and thus less than the mass increase presumed to be due to the metal coating. Indeed, **when** inspecting Figures 22 through 27, a remainder of the deposited metal layer can still be found surrounding the downstream edges of the decelerator grid apertures, while virtually no erosion was visible on the exposed carbon-carbon surfaces. Mass losses from the accelerator grids are more pronounced but still very small, around 0.26-0.27 gm. Combined losses from all three grids are 0.31 gm for grid set A and 0.28 gm from set C. Referenced to the total mass of the three grids, this corresponds to a mass loss of 0.35% of grid set A and 0.3% for set C. Since furthermore no obvious grid thickness changes were noted between **pre-** and post test conditions, mass losses of this magnitude can only be caused by direct ion impingement. As was mentioned earlier, evidence of direct ion impingement was found when inspecting grid hole wear patterns (see Fig. 21). The mass increase of the screen grids is likely the result of both carbon deposits from the various grids, mainly the accelerator grid, and metal deposits found near the edges of the upstream side of the screen grid shown in Figures 52 and 53, **backsputtered** from the discharge chamber walls. Screen grid erosion from the discharge chamber plasma therefore appears to be very low, indicating that screen grid life is not an issue.

PART II: FABRICATION OF ADVANCED CARBON-CARBON PANELS

Motivation

During previous testing of carbon-carbon grid sets described above and in Reference 9, it was noted that **perveances** obtained with those grids were lower than those obtainable with molybdenum grids of comparable open area fraction and grid separations. The cause for the slightly lower **perveance** limit of the carbon-carbon grid sets tested was believed to be the larger thickness of the grids. The previously used carbon-carbon accelerator and decelerator panels had thicknesses around 0.95 mm, while corresponding molybdenum thicknesses were only about 0.38 mm. Thus, ions have to travel through “longer” apertures in the thicker **carbon-**carbon grids and suffer a higher probability of impinging on the wall surface areas, reducing the extractable beam current from the grid and therefore lowering its **perveance**.

Reducing grid thicknesses for carbon-carbon grids, however, would lead to a reduced rigidity of those grids in particular for the high open area screen grid, unless steps are undertaken in the manufacturing of those grid panels to increase their stiffness. The critical parameter for ion engine grids here is the **flexural** modulus. A high **flexural** modulus for a grid will result in the grid being able to better resist the electrostatic attraction forces between the different grids of the set, held at different grid potentials. In addition, stiffer grids will also be better suited to resist structural launch loads for an actual flight system. In the following sections, the fabrication of advanced 15-cm and 30-cm carbon-carbon panels will be discussed. As mentioned earlier, budgetary restraints did not allow for a completion of the grid sets. No grid apertures were drilled into the carbon-carbon panels to date, however, the panels are available for completion of the fabrication process should the funding situation improve.

Panel Fabrication

15-cm Panels

The carbon-carbon panels went through several stages of fabrication, consisting on tape lay-up, curing, carbonization, **graphitization** and chemical vapor infiltration (**CVI**). Commercial prepreg tape from YLA Inc., consisting of DuPont E55 fiber made from pitch based carbon and **phenolic** resin (Borden **SC1008 phenolic**) was used for the panel lay-up. Two different types of lay-ups were fabricated. The first lay-up was of the $[0^\circ/+60^\circ/-60^\circ]_s$ type used for conventional carbon-carbon grids using circular apertures. The second lay-up was of a $[0^\circ/0^\circ/90^\circ]_s$ type and was used later in the fabrication of four slotted grids, described in a companion **paper**¹ 8. The lay-up for both sets of panels was performed at JPL. A total of sixteen $[0^\circ/+60^\circ/-60^\circ]_s$ panels and twelve $[0^\circ/0^\circ/90^\circ]_s$ panels were fabricated. Following the lay-up, the panels are still flexible at room temperature and exhibit a considerable amount of “tack” due to the **prestage-cured** resin content of the prepreg material.

Curing of the composite lay-up was performed in a 1.5 m diameter, liquid CO₂ pressurized Baron autoclave, located at the JPL Edwards facility at Edwards AFB. The panels were prepared for curing as shown in Fig. 55. The composite lay-up is placed between two aluminum caul plates, with the upper caul plate applying pressure to the lay-up to ensure that it stays flat. Both aluminum plates and the lay-up are then placed onto a larger, polished aluminum baseplate, which has previously been covered with a **teflon** release film. The release film will allow easy removal of the lay-up from the baseplate, even if excess resin has bled out of the lay-up. Bleeder cloth (fiber glass) is employed over the lay-up and an impermeable vacuum bag is covering the entire set-up. Double-sided tape is sealing the vacuum bag to the aluminum base plate. A hole is cut into the bag and a vacuum hose fitting is placed through it. The bag is then evacuated with the bleeder cloth distributing the vacuum over the entire lay-up. Finally, the entire set-up is placed into the autoclave, pressurized to 300 psi in a CO₂ atmosphere and heated to 110 °C for 30 minutes. Temperature inside the autoclave is then raised to 165 °C for one hour. Then the autoclave is vented and the lay-up is being removed after cooling. Finally, the two caul plates are removed with the panels now rigid,

Following the cure, the panels were delivered to BF Goodrich where they underwent carbonization, graphitization and chemical vapor infiltration cycles. Carbonization takes place at 815 °C and converts the resin content of the cured **prepreg** tape to carbon by releasing its **volatiles**. The carbonization cycle is followed by a graphitization cycle at 3000 °C to graphitize the carbon and increase strength and stiffness of the panels. The very high graphitization temperature was used to obtain maximum stiffness of the panels. During carbonization and graphitization cycles, the matrix forms microcracks because of weight loss and densification (release of volatile). These voids are now being filled in a carbon vapor infiltration cycle, where carbon is deposited over the composite. The particular CVI cycle used in the fabrication of these panels is proprietary to BF Goodrich. Finally, a second graphitization cycle at 3000 °C is employed to graphitize the CVI deposited carbon and a last **CVI** cycle is used to close cracks left by the last graphitization.

Table 8 shows some of the material properties of the new carbon carbon panels (both $[0^\circ/+60^\circ/-60^\circ]_s$ and $[0^\circ/0^\circ/90^\circ]_s$ lay-up) when compared with carbon-carbon panels of the second generation, such as those used in the endurance and permeance tests. Remarkable is the high fiber volume and the corresponding low carbonized resin content in the third generation $[0^\circ/+60^\circ/-60^\circ]_s$ panels, resulting in the strongest quasi-isotropic carbon-carbon material ever made. The marked increase for the value of the **flexural** modulus over the corresponding value of the second generation panels is especially noteworthy. As was pointed out earlier, the **flexural** modulus is a critical grid structural property since it determines how far the grid may bend due to electrostatic or vibrational (launch) loads. The carbon-carbon value for the **flexural** modulus in the **0°** direction now reaches about 80% of the value for molybdenum. However,

this increase in **flexural** modulus in the 0° direction comes at a price. Due to the higher fiber volume of these panels, less cross-linkage is provided by the reduced matrix content and the **flexural** modulus in the 90° direction is thus reduced over the value found for the second generation panels.

Even more remarkable is the value for the **flexural** modulus of the [0°/ 0°/90°]_s panels that reach the value found for molybdenum in the 0° direction. However, since two thirds of the fiber material is oriented in the 0° direction and only one third in the 90° direction, **flexural** modulus values are relatively small that direction, These panels are thus stiff in the 0° direction but bend easily in the 90° direction. This fact has been exploited in the fabrication of grids with non-circular, slotted apertures and is discussed in a companion **paper**¹⁸.

Table 8: Materials Properties of Carbon-Carbon Panels

Property	2nd Generation	3rd Generation	
		[0°/+60°/-60°] _s	[0°/ 0°/90°] _s
Density (g/cm ³)	1.77	1.83	1.89
Thickness (mm)	0.5(1)/0.95(2)	0.46	0.48
Fiber by Weight	50.2%	69%	57%
Resin by Weight	17.6%	3-4%	10%
CDI by Weight	32.2%	26-28%	32%
Fiber Volume	40.1%	57%	50%
Resin Volume	16.4%	3%	10%
CDI Volume	30.0%	27%	31%
Void Volume	13.6%	13%	9%
Tensile Strength (M Pa)	308	486(3)	754(3) / 414(4)
Tensile Modulus (GPa)	179	145(3)	230(3) / 121(4)
Flexural Strength (MPa)	240(1) / 280(2)	205(3) / 117(4)	289(3) / 50(4)
Flexural Modulus (GPa)	210(1) / 161(2)	275(3) / 61(4)	340(3) / 21(4)

(1)Screen Grid

(2)Accelerator/Decelerator Grid

(3)0° Direction

(4)90° Direction

30-cm Panels

A set of 30-cm, dished grid panels was fabricated to be used in the fabrication of carbon-carbon grid sets retrofittable to the 30-cm NSTAR engine. The panel lay-up was similar to the lay-up procedure for the 15-cm panels and the same prepreg material was used. Preparation for curing, however, differed due to the desired dished shape the panels were to obtain. For this purpose, graphite molds were machined out of G540 graphite (Tokai Carbon Inc.). Each grid panel required two graphite molds, one female (concave) and one male

(convex) mold shown in Fig. 56. For preparation for curing, the composite lay-up, still flexible at this point, was placed on the female graphite mold and bagged just as the 15-cm panels. When applying vacuum, the outer bag would press the composite lay-up to the female mold and press it in shape as shown in Fig. 57. The panels then underwent the same curing cycle as the 15-cm panels. Figure 58 shows six dished 30-cm carbon-carbon panels after removal from the autoclave, still positioned on their female graphite molds.

The dished panels were then delivered to **BF Goodrich** to undergo the same carbonization, **graphitization** and CVI cycles as the flat 15-cm panels. A major difference between the procedures for the flat and dished panels was that the dished panels remained on their graphite molds during these processes in order to maintain their dished shape. Special graphite molds had been fabricated for the CVI process, allowing the carbon vapor to penetrate the mold and reach the grid panel. The necessity to use molds during these high temperature carbonization and **graphitization** processes had required the selection of graphite for the molds. The dished carbon-carbon panels were too expensive to justify sacrificing a panel for material testing, however, it is assumed that material properties are similar to the ones found for the quasi-isotropic [Oo/+600/-600]s 15-cm panels. Thicknesses for the dished panels were measured around 0.46 mm. Screen grid panels, which have a somewhat smaller diameter, weigh around 95 gm whereas accelerator and decelerator panels weigh around 108 gm and 105 gm, respectively.

Mount Ring Fabrication

In order to save weight for the total assembly, a carbon-carbon mount ring was fabricated for the 30-cm grid set. A photograph of the mount ring is shown in Fig. 59. The mount ring was laid up from segments of plain weave fabric made from PAN based Amoco T-300 fiber and **phenolic** resin (Borden SC1008). Segments of the plain weave fabric are still visible in the finished product, shown in a closer view in Fig. 60. The lay-up and curing was performed with the help of an aluminum fixture shown in Figures 61 and 62, both assembled and disassembled. The mount ring was laid up in the U-shaped crevice formed by the fixture, giving the ring its shape. After completion of the lay-up, a long slab of silicon rubber was inserted into the crevice over the composite lay-up and fixated with a large hose clamp. The entire assembly was then placed in a circulated air oven at 175 °C for 16 hours for curing. Pressure was provided by thermal expansion of the silicon mandrel, however, was not measured.

The mount ring was then removed from the aluminum fixture and further processing was again performed at **BF Goodrich**. The mount ring was processed free-standing during all the following fabrication cycles since the aluminum fixture **would** not have been able to stand up to the heat loads encountered in the subsequent processes. Following a carbonization cycle at 815 oC, **graphitization** took place at 1800 oC. A lower **graphitization** temperature had to be chosen than for the panel since the T-300 fiber material would have distorted at higher temperatures. The **graphitization** cycle was then followed by a CVI cycle, another graphitization cycle and a final CVI cycle, just as the grid panels, except at lower **graphitization** temperatures as discussed. The mount ring would require further machining to the required final dimensions and tolerances as soon as future funding becomes available.

CONCLUSIONS

Two sets of carbon-carbon grids were subjected to a 700 hour endurance test. Carbon-carbon grid erosion was minimal stressing carbon-carbon's remarkable capabilities as the material of choice for long-life grid applications. The grids were visually inspected by means of an electron microscope. A layer of molybdenum and tungsten, that had coated the grids as a results of **backsputtering** from a probe rake used in a previous experiment, was eroded in the familiar "groove" and "pit" areas on the grid. However, the underlying carbon-carbon composite surface appeared to have suffered virtually no erosion. Some delamination on the downstream side of the decelerator grid had occurred at locations where fiber directions were normal to the hole edge. However, it was unclear from the visual inspection, whether this delamination had occurred early in the endurance tests or before the tests, possibly during fabrication. The decelerator grid was mechanically drilled and drill bits are known to cause delamination of a composite at the exit side of the drill. Evidence of carbon redeposition was found on the grids, particularly on the downstream sides of the screen and accelerator and the upstream side of the decelerator grid, as well as on the wall surfaces of decelerator and accelerator grid holes, predominantly toward the edges of the grids. X-ray fluorescence scans revealed traces of xenon trapped in those deposits. On the upstream side of the screen grid, close to its edges, metal deposits were found. X-ray fluorescence of those deposits seemed to indicate that those deposits resulted from discharge chamber erosion and redeposition of **backsputtered** material on the screen grid at the described locations.

Measurements of grid mass losses showed that losses were minimal from all grids, 0.1 gm in the case of the decelerator and screen grids and 0.25 to 0.26 gm in the case of the accelerator grids. Mass losses could not be correlated with reductions in grid thickness. Grid thickness measurements both before and after the test **revealed** that any reductions in thickness, should they have occurred, were well within the margin of error of the measurements. However, some enlargement of grid hole apertures were found, in particular for the accelerator grids. Changes in hole diameters were still small, though, and on the order of 60 to 70 μ m for the accelerator grid of grid set A and 35 to 45 μ m for set C. Carbon redeposits at hole wall surfaces appeared to have been responsible for some of the holes to have reduced in diameter, in particular closer to the edges of the grid.

Perveance testing the two sets of carbon-carbon grids prior to the endurance test showed a slightly reduced **perveance** limit of the carbon-carbon grids over molybdenum grids of the same open area fraction and grid gap spacing. The **perveance** limits of carbon-carbon were about 100 V higher than those of the molybdenum grids. This was attributed to the larger thickness of the carbon-carbon accelerator and decelerator grids. This grid thickness was 0.95 mm for carbon-carbon, but only 0.38 mm for molybdenum.

Efforts to further increase carbon-carbon grid **perveances** led to the fabrication of advanced, thin carbon-carbon grid panels with fiber volume fractions as high as 57%. The high fiber volume is necessary to increase the strength and stiffness of the grid. Sixteen 15-panels of a $[0^\circ/+60^\circ/-60^\circ]_s$ lay-up and twelve of a $[0^\circ/0^\circ/90^\circ]_s$ lay-up were manufactured. The current batch of panels represents some of the strongest carbon-carbon ever made, approaching values for the **flexural** modulus equal to that of molybdenum. The **flexural** modulus is a critical grid structural property, since it describes how well a grid may resist electrostatic and vibrational loads. A set of dished 30-cm carbon-carbon panels as well as a carbon-carbon mount ring to support the dished grid set were fabricated. The carbon-carbon material is of the same high stiffness as the one used for the fabrication of the 15-cm $[0^\circ/+60^\circ/-60^\circ]_s$ panels. The 30-cm grid set is designed to be **retrofittable** to the 30-cm NSTAR engine, providing it with a **ultra-long-life** capability.

ACKNOWLEDGEMENTS

The authors would like to thank Mr. Alison Owens, Mr. William Thogmarten and Mr. Robert Toomath for their invaluable help throughout this project, Special thanks also goes to Mr. Jim **Kulleck** who performed the electron microscope and x-ray **fluorescence** scans. The work described in this paper was performed at the Jet Propulsion Laboratory, California Institute of Technology, under contract with the National Aeronautics and Space Administration,

This paper is dedicated in memory of Mr. Lewis **Pless**. Lew passed away on January 1, 1995. His electronic skills and knowledge helped make this project possible, We will miss him.

REFERENCES

1. Polk, J. E., Moore, N. **R.**, **Newlin**, L. E., Brophy, J. R., and **Ebbeler**, D. H., "Probabilistic Analysis of Ion Engine Accelerator Grid Life", **IEPC** Paper 93-176, 23rd International Electric Propulsion Conference, Seattle, WA, Sep. 13-16, 1993.
2. Brophy, J. R., Polk, J.E., and L. C. **Pless**, "Test-to-Failure of a Two-Grid, **30-cm-dia.** Ion Accelerator System", **IEPC** Paper 93-172, 23rd International Electric propulsion Conference, Seattle, WA, Sep. 13-16, 1993.
3. NASA Strategic Plan, National Aeronautics and Space Administration, Washington, D. C., February 1995.
4. The JPL Strategic Plan, JPL Internal Document, JPL 400-549, Pasadena, CA, April 1995.
5. **Sauer**, C. G., "Planetary Mission Performance for Small Solar Electric Propulsion Spacecraft", Paper AAS 93-561, Astrodynamics Specialists Conference, Victoria, Canada, August 16-19, 1993.
6. **Sauer**, C.G. and Yen, C-W.L., "Planetary Mission Capability of Small Low power Solar Electric Propulsion Systems", **IAA** Paper 1-0706, **IAA** International Conference on Low-Cost Planetary Missions, Johns Hopkins University Applied Physics Laboratory, Laurel, MD, April 12-15, 1994.
7. Kakuda, **R.**, **Sercel**, J., and Lee, W., "Small Body Rendezvous Mission using Solar Electric Propulsion: Low Cost Mission Approach and Technology Requirements", IAA Paper L-07 10, IAA International Conference on Low-Cost Planetary Missions, Johns Hopkins University Applied Physics Laboratory, Laurel, MD, April 12-15, 1994.
8. **Tucci**, L., "Report: NASA lags in Research Investment, Technology Use", *Space News*, Vol. 5, No. 24, June 20-26, 1994, pp. 3.
9. Mueller, J., Brophy, J. R., Brown, D. K., and Garner, C. E., "Performance Characterization of 15-cm Carbon-Carbon Composite Grids", AIAA Paper 94-3118, 30th Joint Propulsion Conference, Indianapolis, IN, June 27-29, 1994.

10. Mueller, J., Brown, D. K., Garner, C.E., and Brophy, J. R., "Fabrication of Carbon-Carbon Grids for Ion Optics", IEPC Paper 93-112, 23rd International Electric Propulsion Conference, Sep. 13-16, 1993, Seattle, WA.
11. Garner, C.E. and Brophy, J. R., "Fabrication and Testing of Carbon-Carbon Grids for Ion Optics", AIAA Paper 92-3149, 28th Joint Propulsion Conference, Nashville, TN, July 6-8, 1992.
12. Meserole, J.S. and Hedges, D.E., "Comparison of Erosion Rates of Carbon-Carbon and Molybdenum Ion Optics", IEPC Paper 93-111, 23rd International Electric Propulsion Conference, Seattle, WA, Sept. 13-16, 1993.
13. Hedges, D.E. and Meserole, J. S., "Demonstration and Evaluation of Carbon-Carbon Ion Optics", *Journal of Propulsion and Power*, Vol. 10, No. 2, March-April 1994, pp.255-261.
14. Meserole, J. S., "Measurement of Relative Erosion Rates of Carbon-Carbon and Molybdenum Ion Optics", AIAA Paper 94-3119, 30th Joint Propulsion Conference, June 27-29, 1994, Indianapolis, IN.
15. Brown, D.K. and Garner, C. E., "Carbon/Carbon for Ion Optics", JANNAF Joint Propulsion Meeting, November 1993.
16. Blandino, J. J., Goodwin, D.G., Garner, C.E. and Brophy, J. R., "Evaluation and Development of Diamond Grids for Ion Optics", AIAA Paper 95-2663, 31st Joint Propulsion Conference, San Diego, CA, July 10-12, 1995.
17. Schwartz, M., "Composite Materials Handbook", 2nd edition, McGraw-Hill, New York, 1992.
18. Brophy, J. R., Mueller, J., and Brown, D. K., "Carbon-Carbon Ion Engine Grids with Non-Circular Hole Apertures", AIAA Paper 95-2662, 31st Joint Propulsion Conference, San Diego, CA, July 10-12, 1995.
19. Brophy, J. R., Mueller, J., Brown, D.K., and Garner, C.E., "Slotted Grids in Carbon-Carbon for Ultra Long-Life Ion Accelerator Systems", New Technology Report NPO-19679/9293, JPL Technology Utilization Office, March 28, 1995.
20. Mueller, J., "Ion Engine Grid using Rectangular Hole Geometries", New Technology Report NPO- 19336/8912, JPL Technology Utilization Office, Oct. 21, 1995.
21. Kaufmann, H. R., "Technology of Electron-Bombardment Ion Thrusters", in Advances in Electronics and Electron Physics, pp.300, Academic Press, New York, 1974.
22. Brophy, J. R., Mueller, J., Pless, L. C., Goodfellow, K. M., and Anderson, J. R., "Segmented Ion Engine Operation and Performance", AIAA Paper 94-2851, 30th Joint Propulsion Conference, June 27-29, 1994, Indianapolis, IN.
23. Brophy, J. R., Pless, L. C., Mueller, J., and Anderson, J. R., "Operating Characteristics of a 15-cm-dia. Ion Engine for Small Planetary Spacecraft", IEPC Paper 93-110, 23rd International Electric Propulsion Conference, Seattle, WA, Sep. 13-16, 1993.

24. **Tierney, M. M.**, Brophy, J. R., and Mueller, J., "Segmented Ion Engine Plume Diagnostics", AIAA Paper 94-2740, 30th Joint Propulsion Conference, June 27-29, **1994**, Indianapolis, IN.
25. Rosenberg, D. and **Wehner, G.K.**, "Sputtering Yields for Low Energy He, Kr, and Xe Ion Bombardment", *J. Appl. Phys.* **33(5)**, 1962, pp. 1842-1845.
26. Oberg, E., Jones, F.D., Horton, H.L., and Ryffel, H.H., "Machinery's Handbook", 24th edition, Industrial Press, New York, 1992.



Fig 1

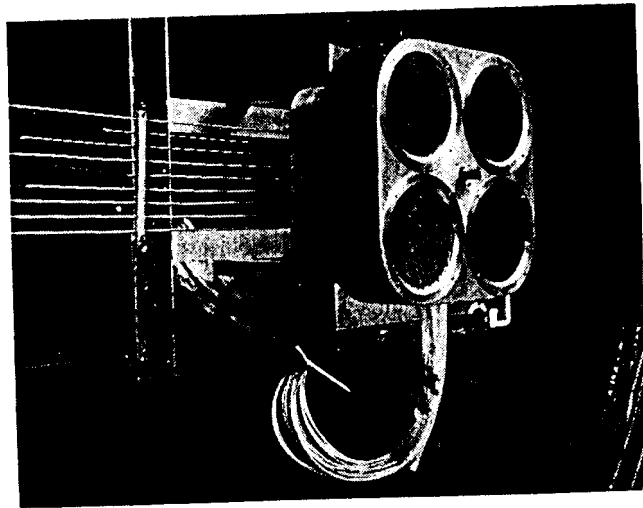


Fig 2

Juergen,
FYI
JRTB

8/2/94

Carbon-Carbon Grid Perveance

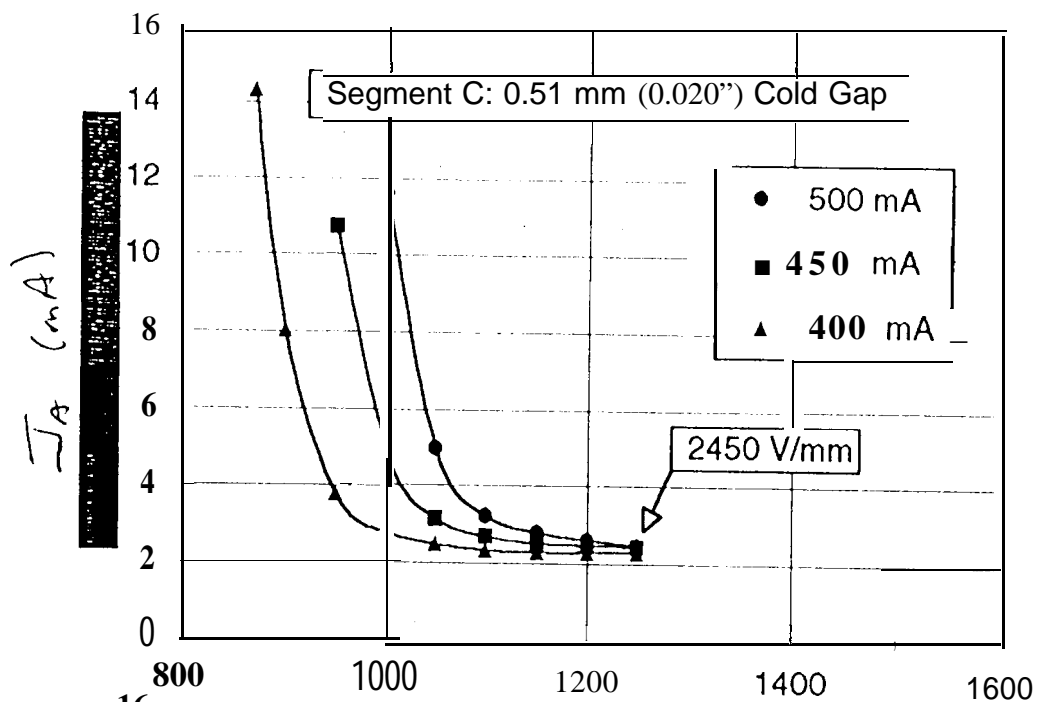


Fig 3

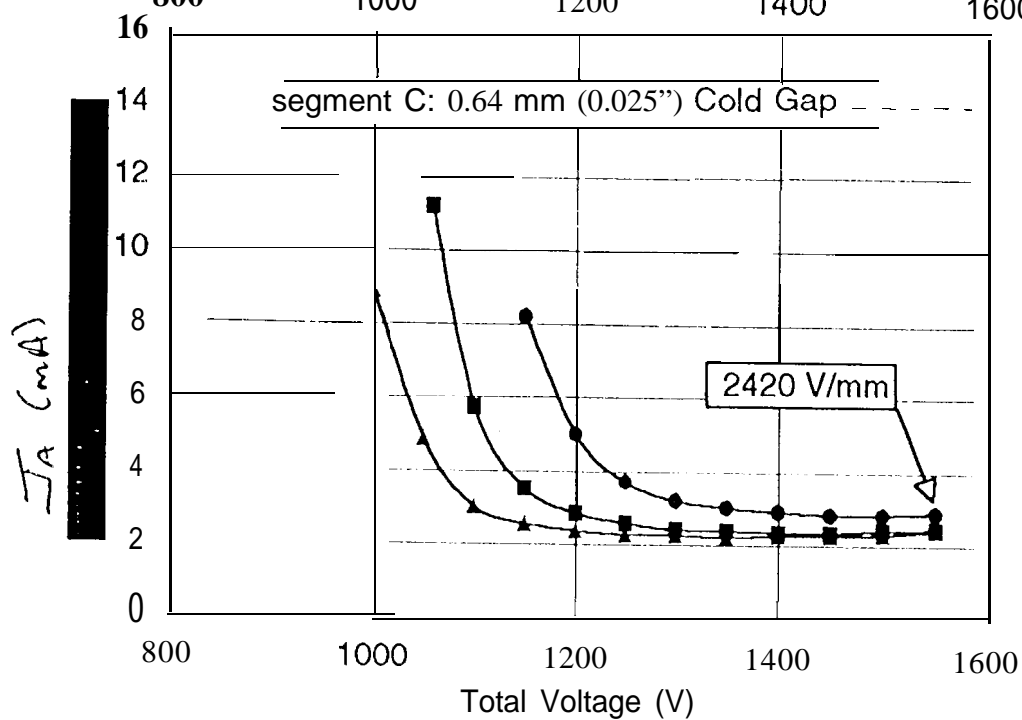


Fig 4

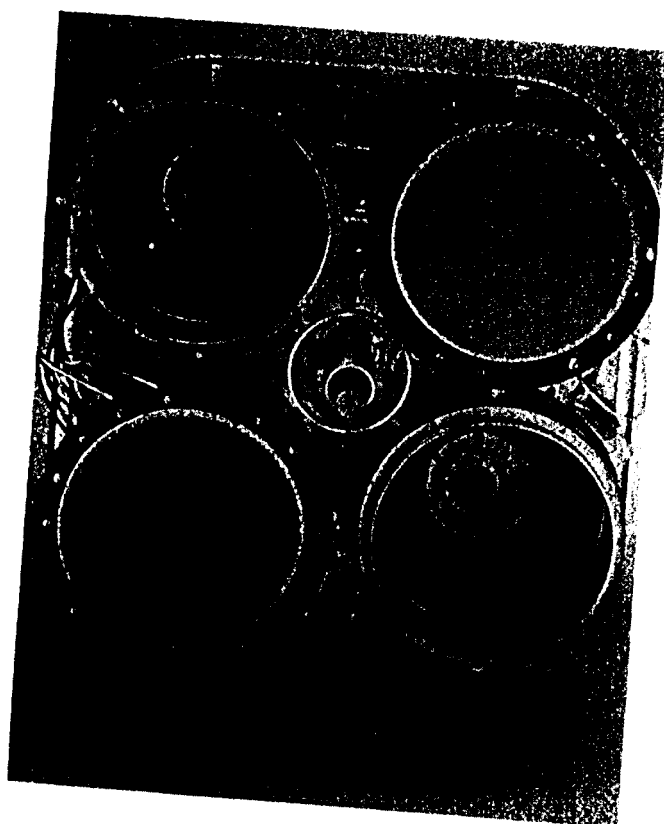


Fig 6

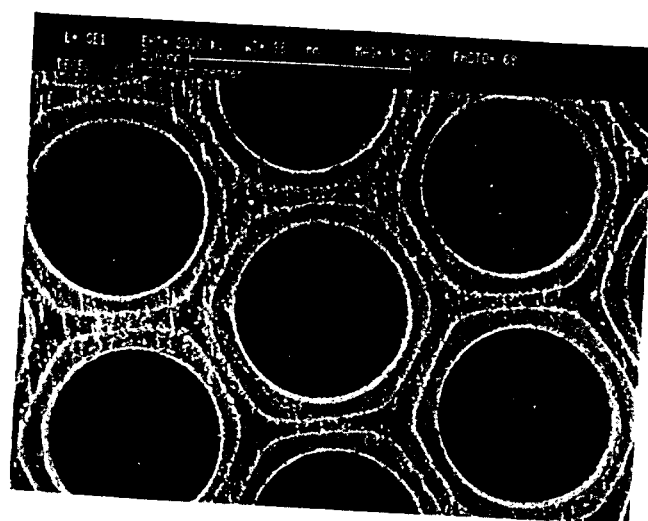


Fig 8

smooth metal. deposit
interface → Deposit - CC

Deal A Downstream

Fig 9

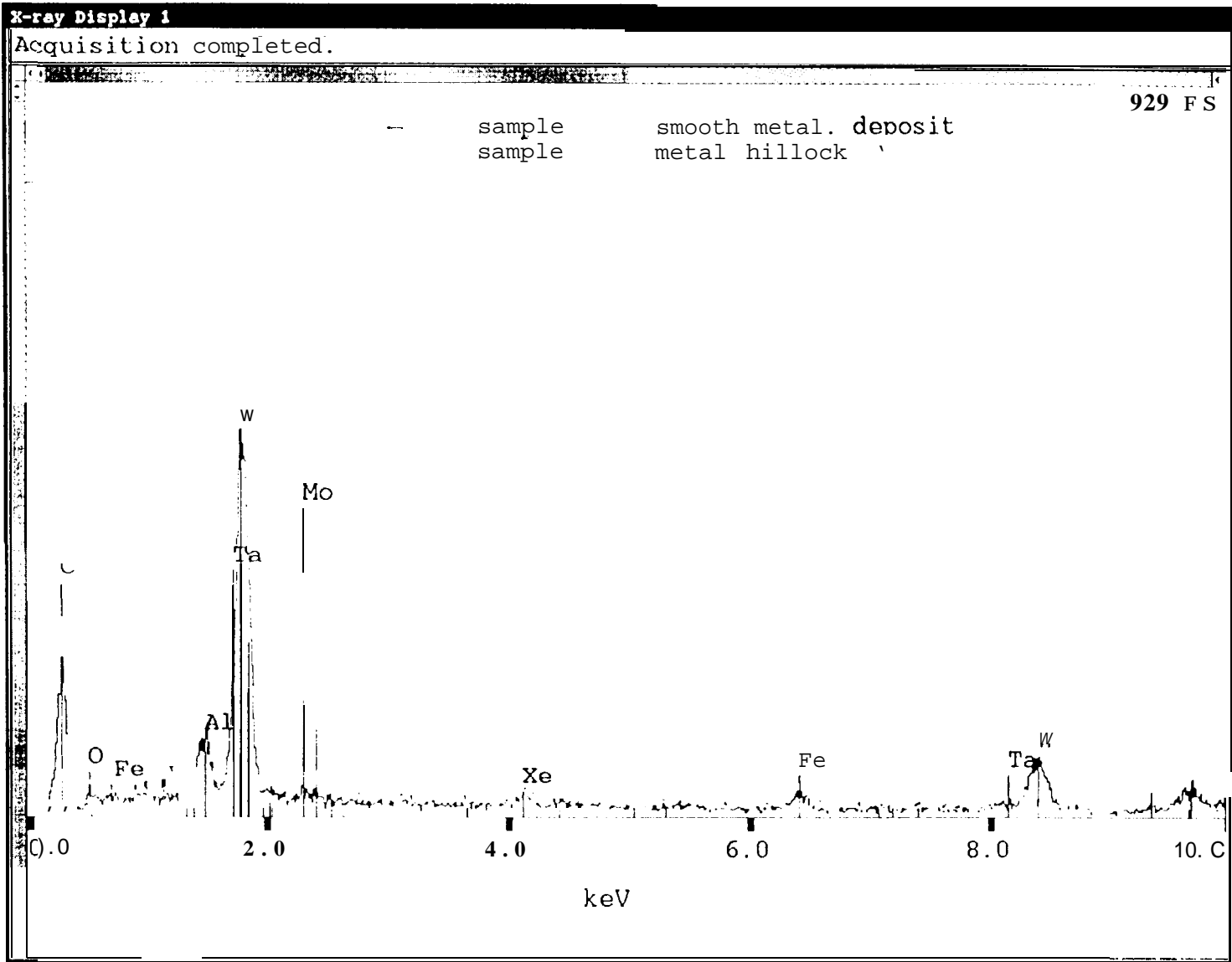




Fig 10

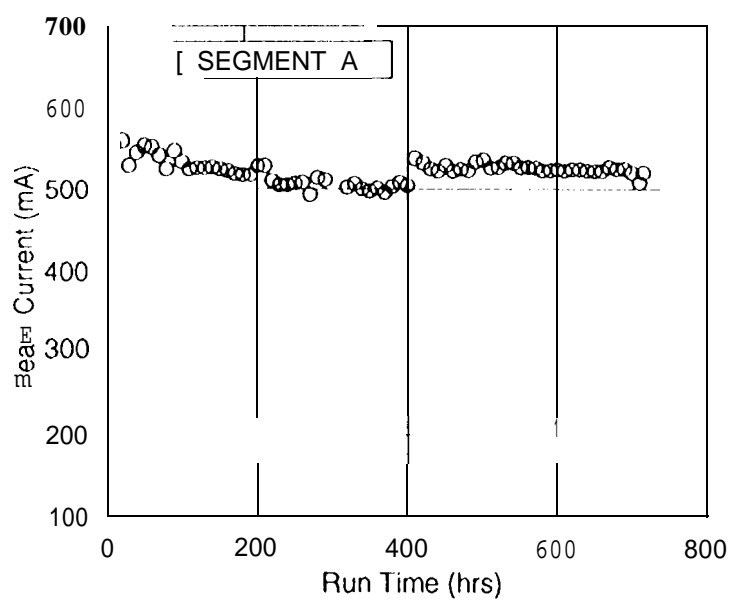


Fig 11

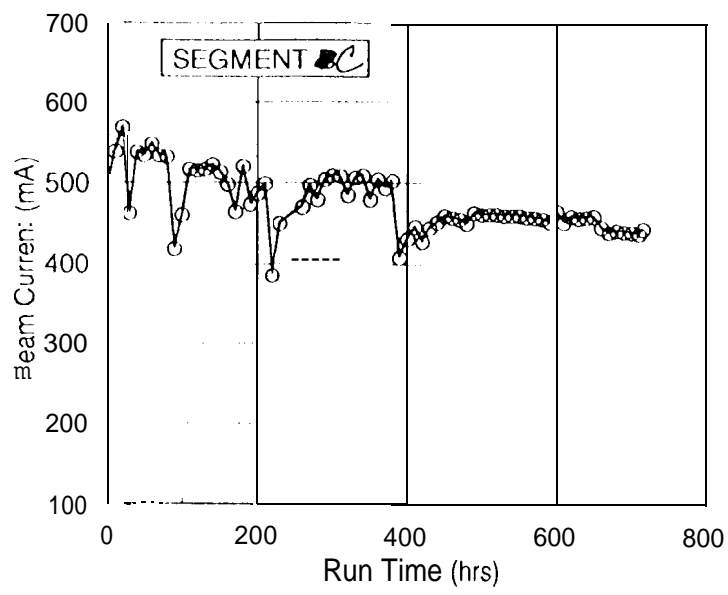


Fig 12

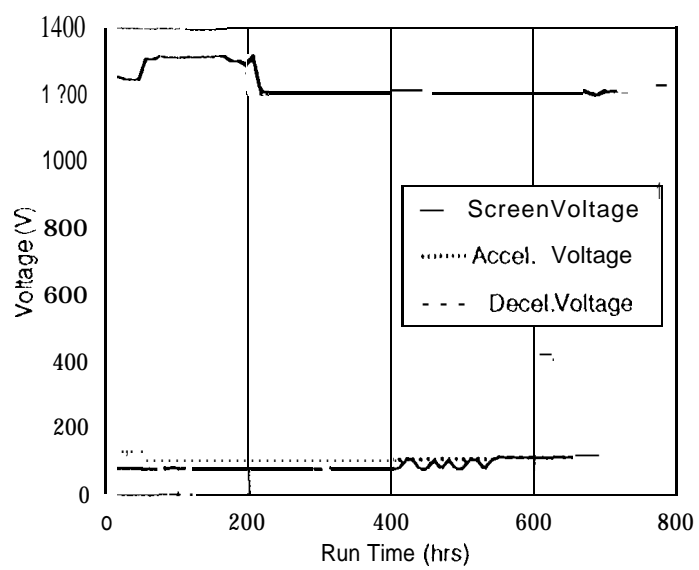


Fig 13

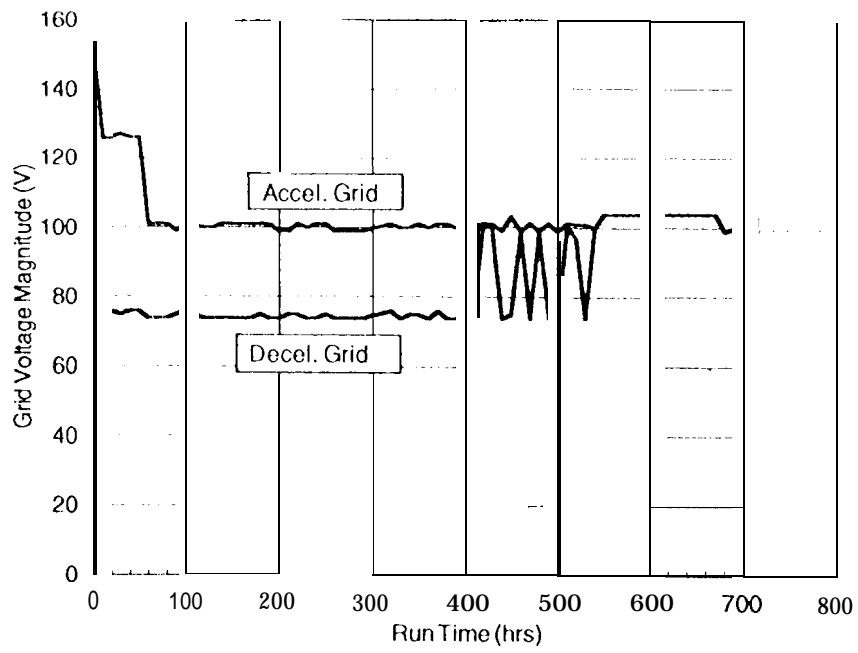
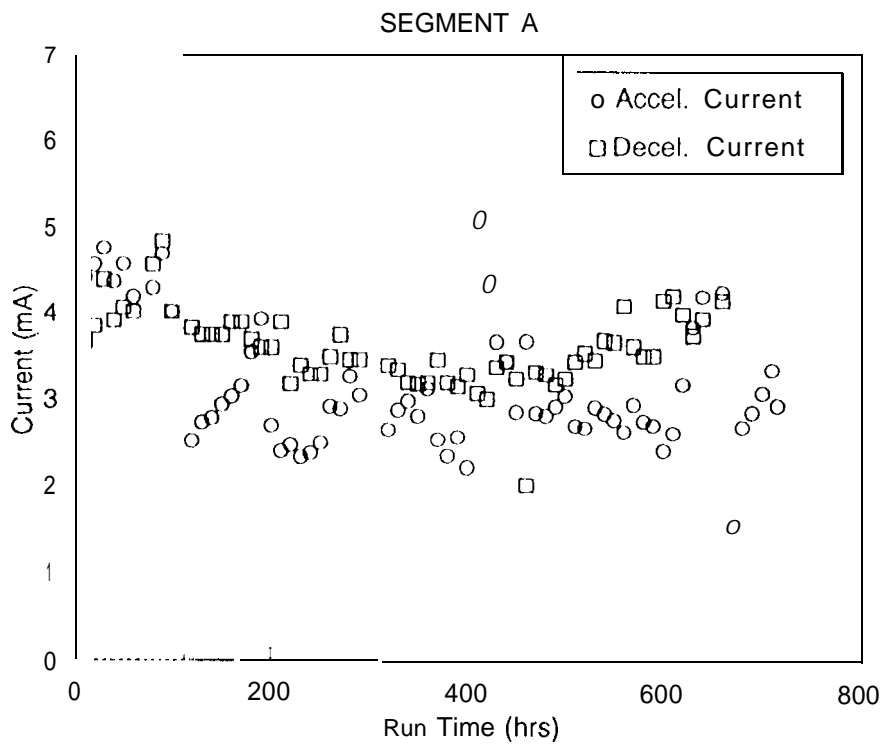


Fig 14



Fy 15

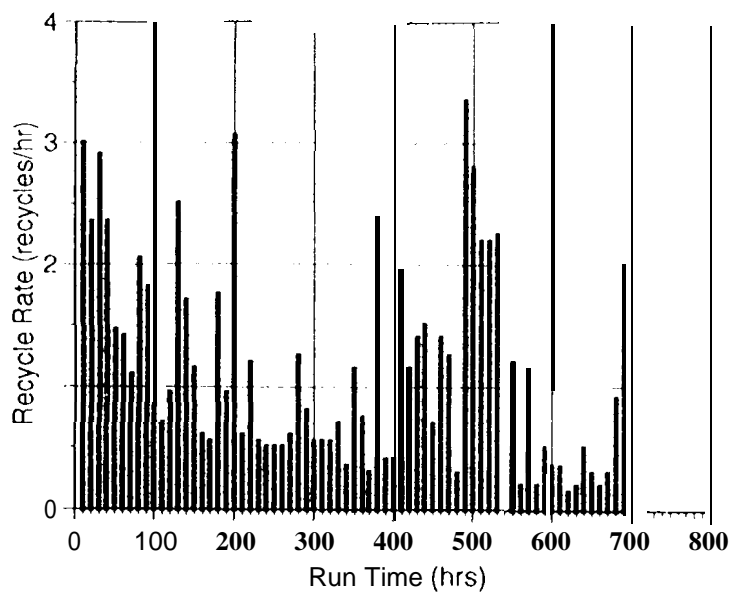


Fig 16

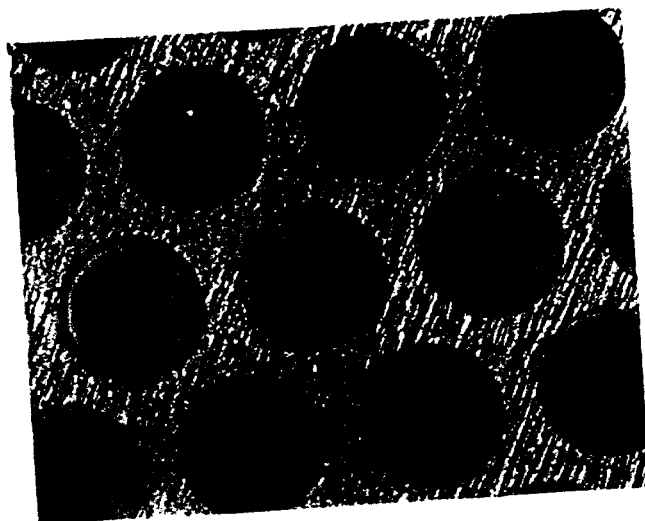


Fig 17

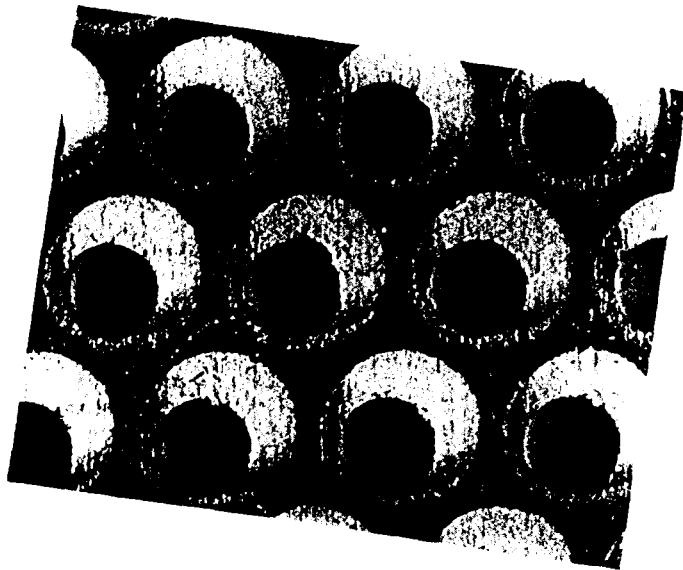


Fig 18

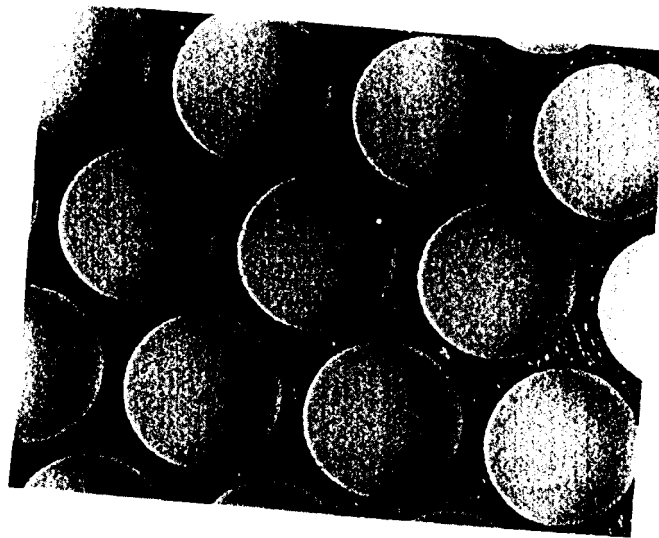


Fig 14

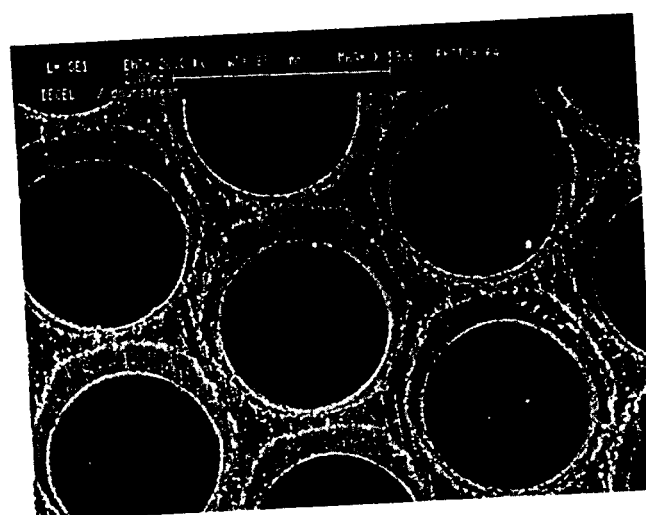


Fig 20

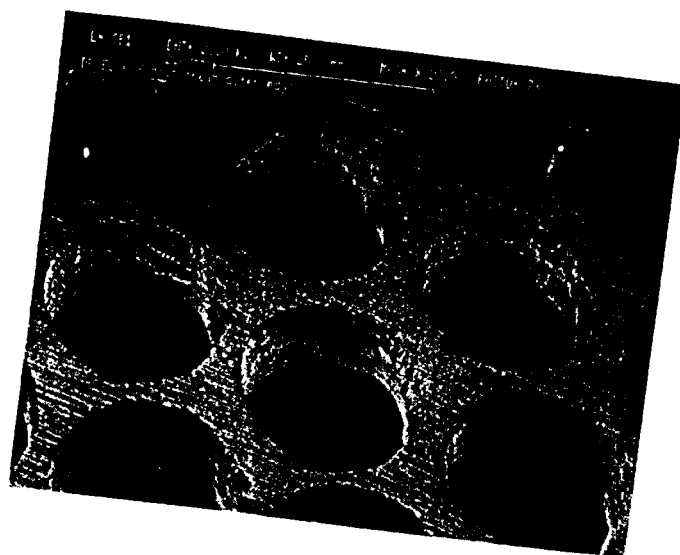


Fig 21

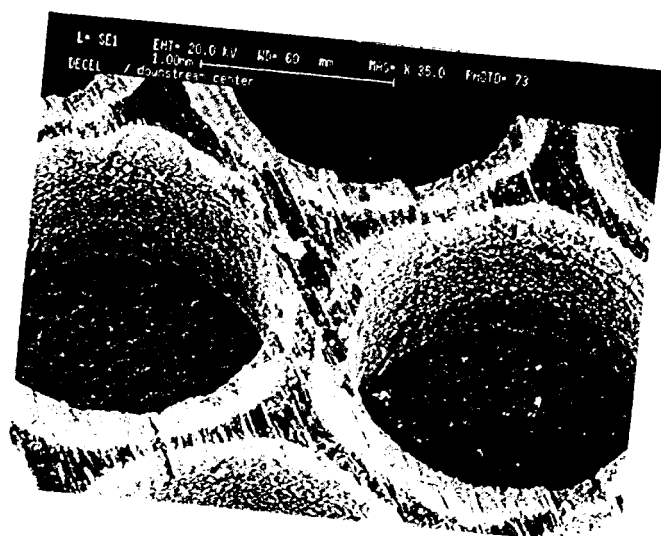
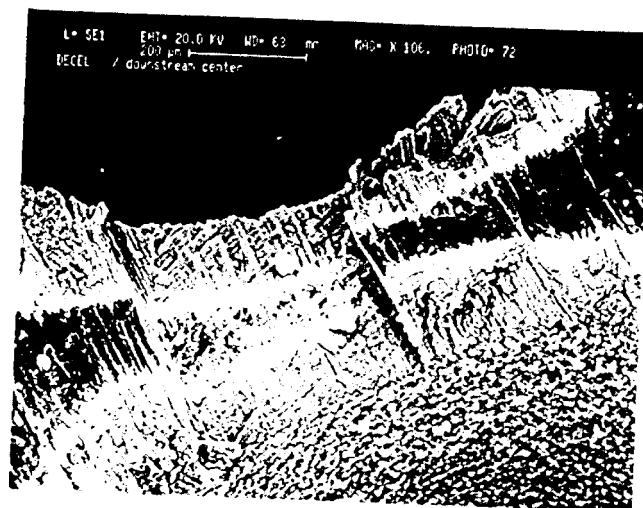
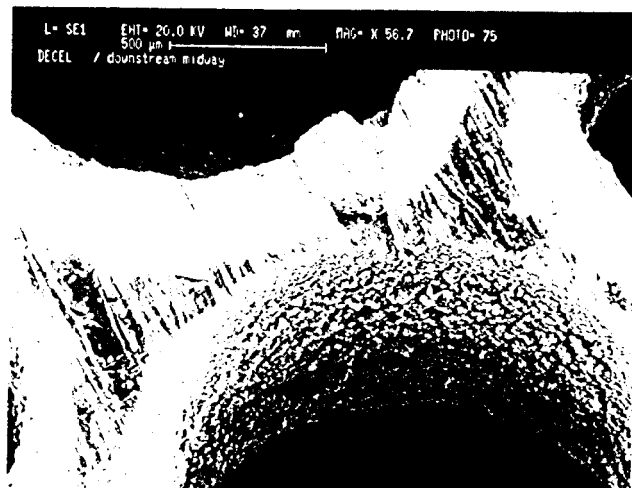


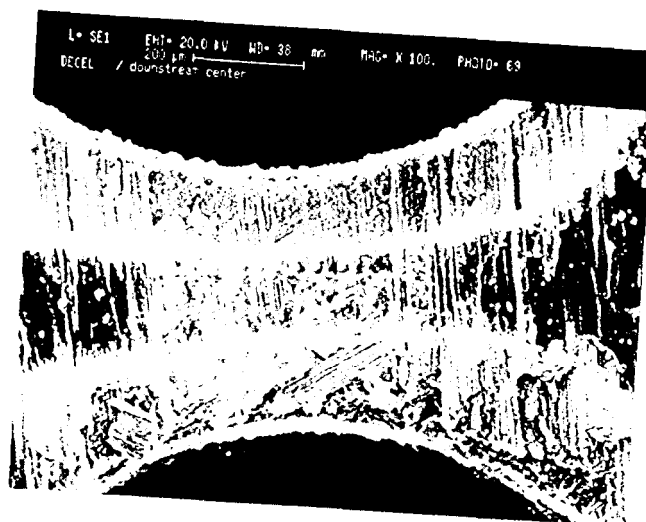
Fig 22



Fj 23



Fj 29



Fj25

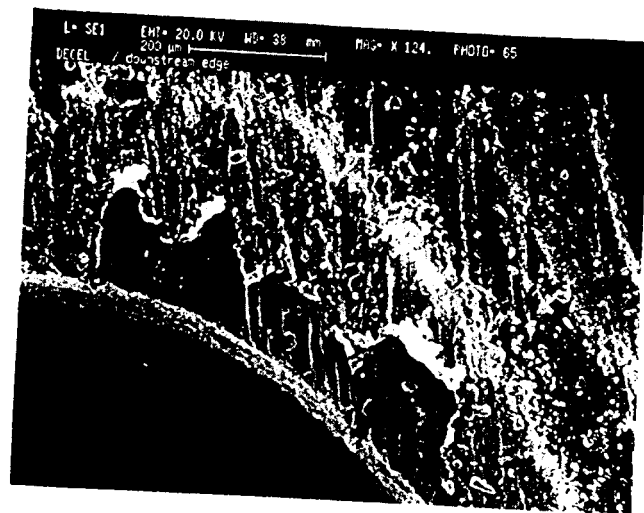


Fig 26

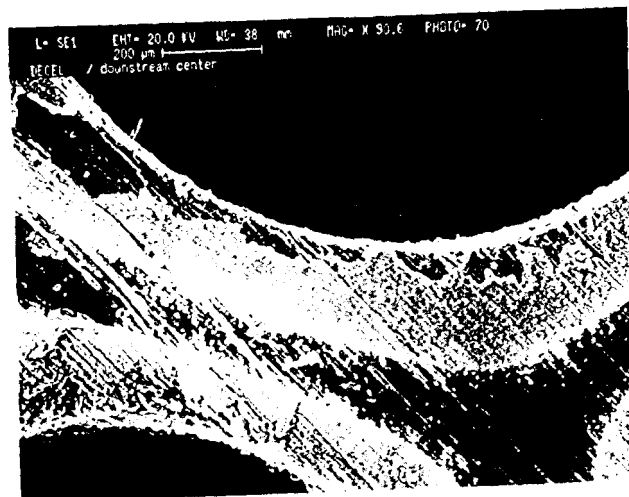
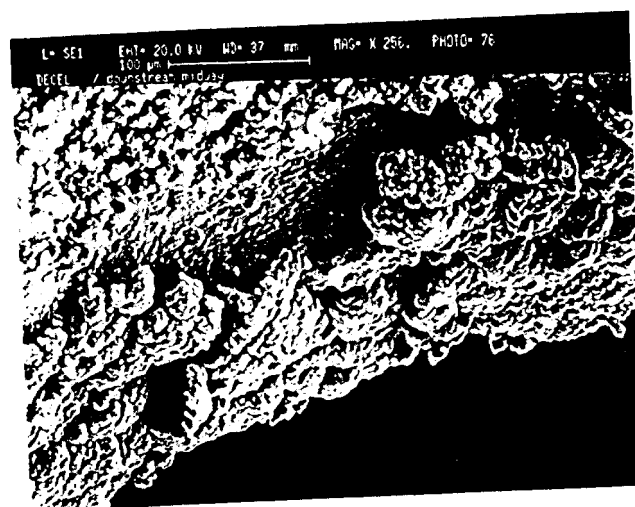


Fig 23

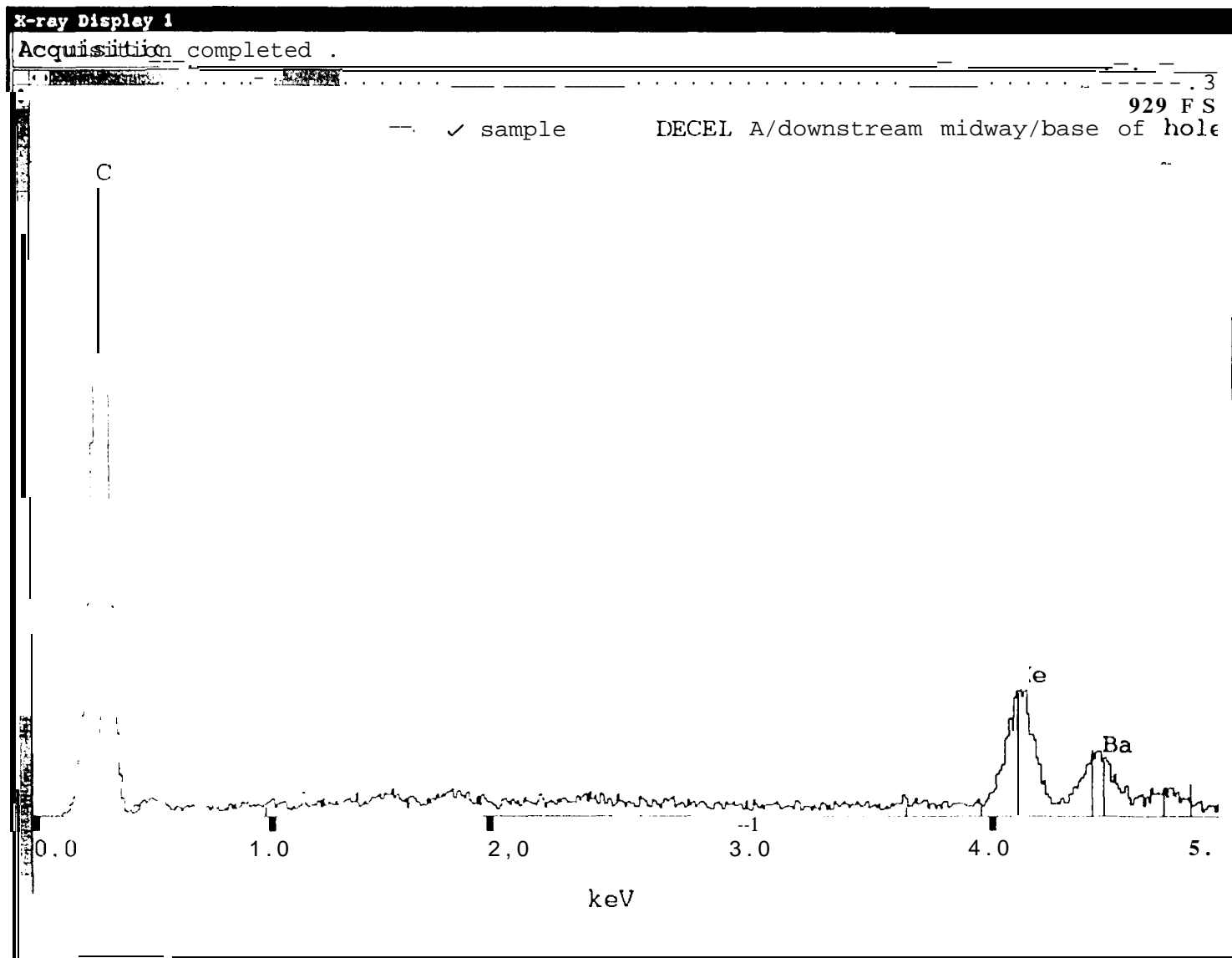


7528

Deposits Deal holes (upstream)

Deal A downstream

Fig 29



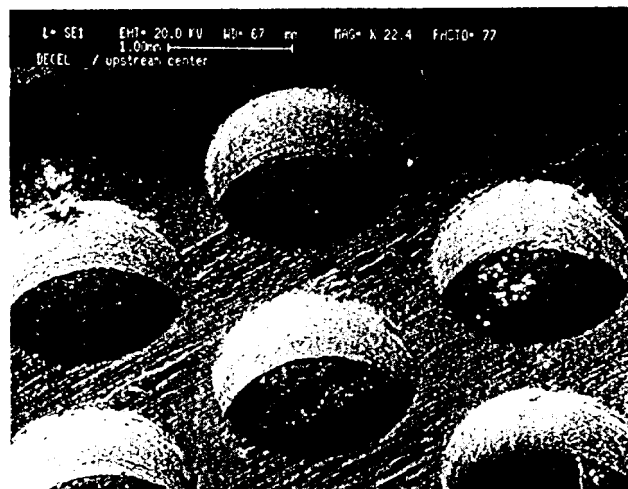


Fig 30

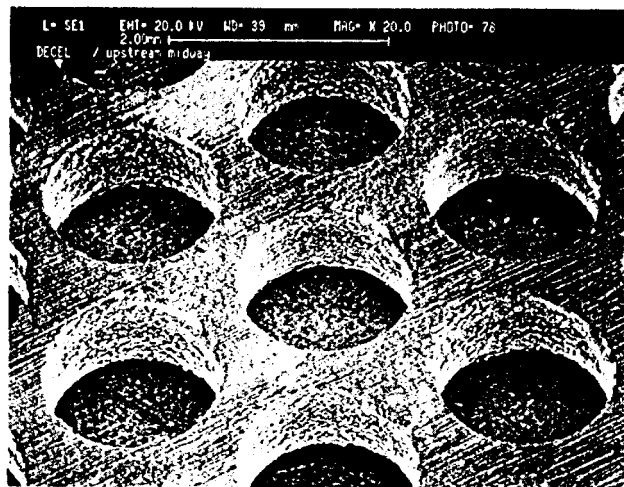


Fig 31

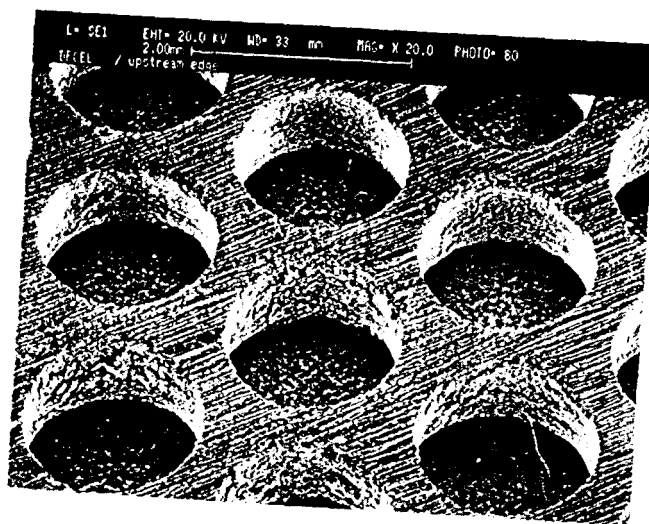


Fig 32

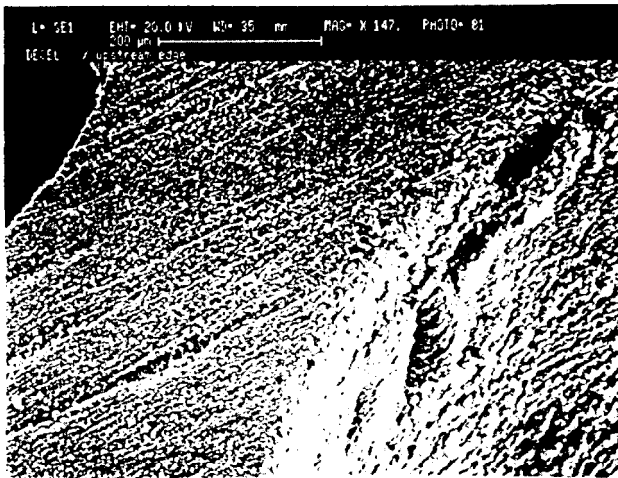
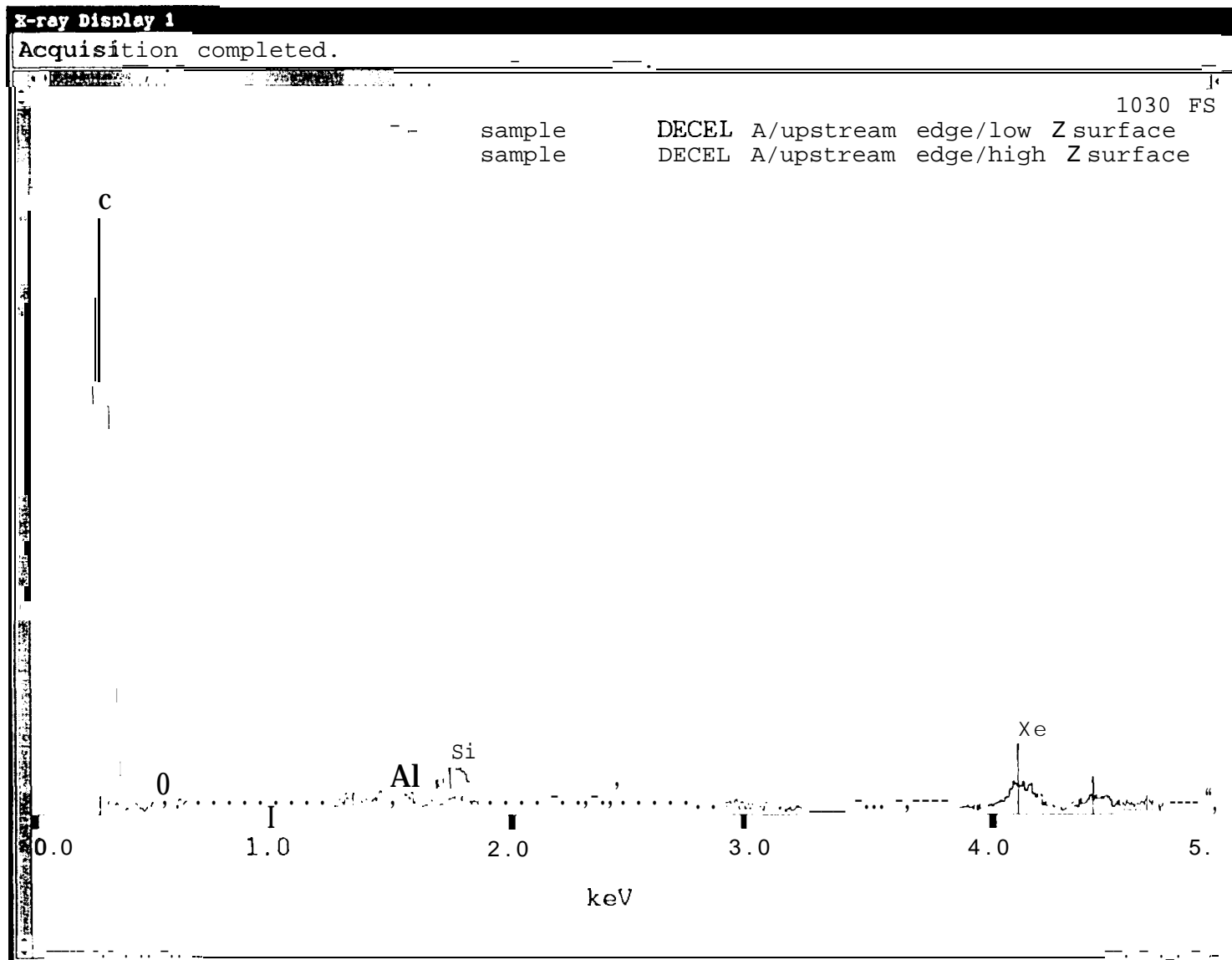
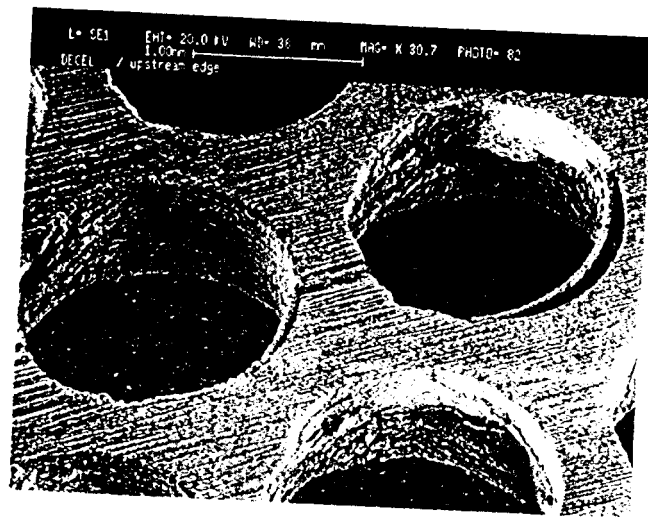


Fig 33

DECEL A UPSTREAM - WGBBING AREA

Fig 34





75 38

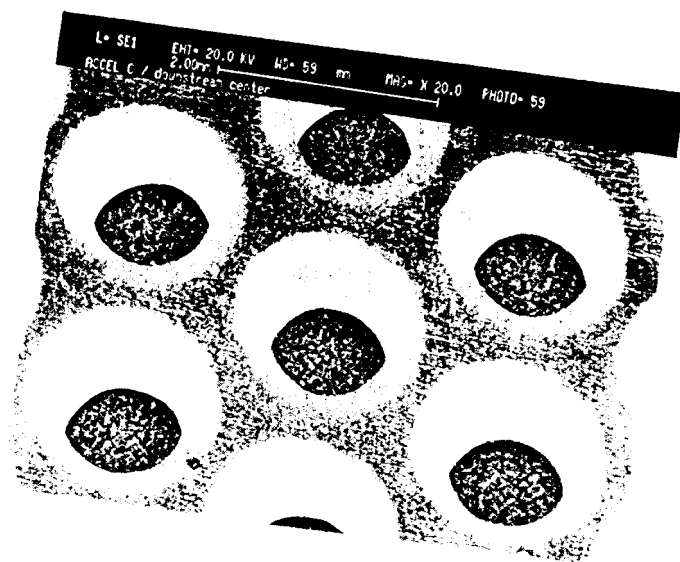


Fig 3c

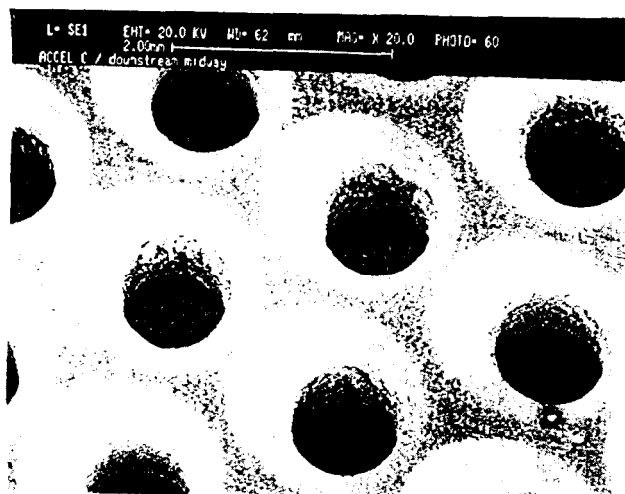


Fig. 37

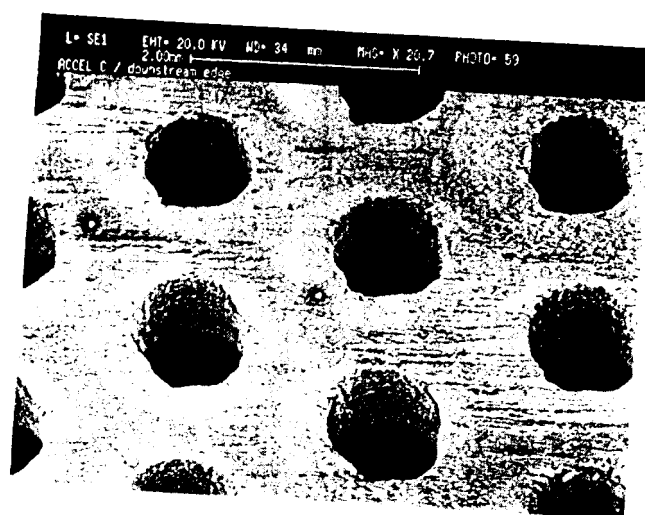


Fig 38

ACCEL C Downstream webbing at edge

Fig 39

X-ray Display 1

Acquisition completed.

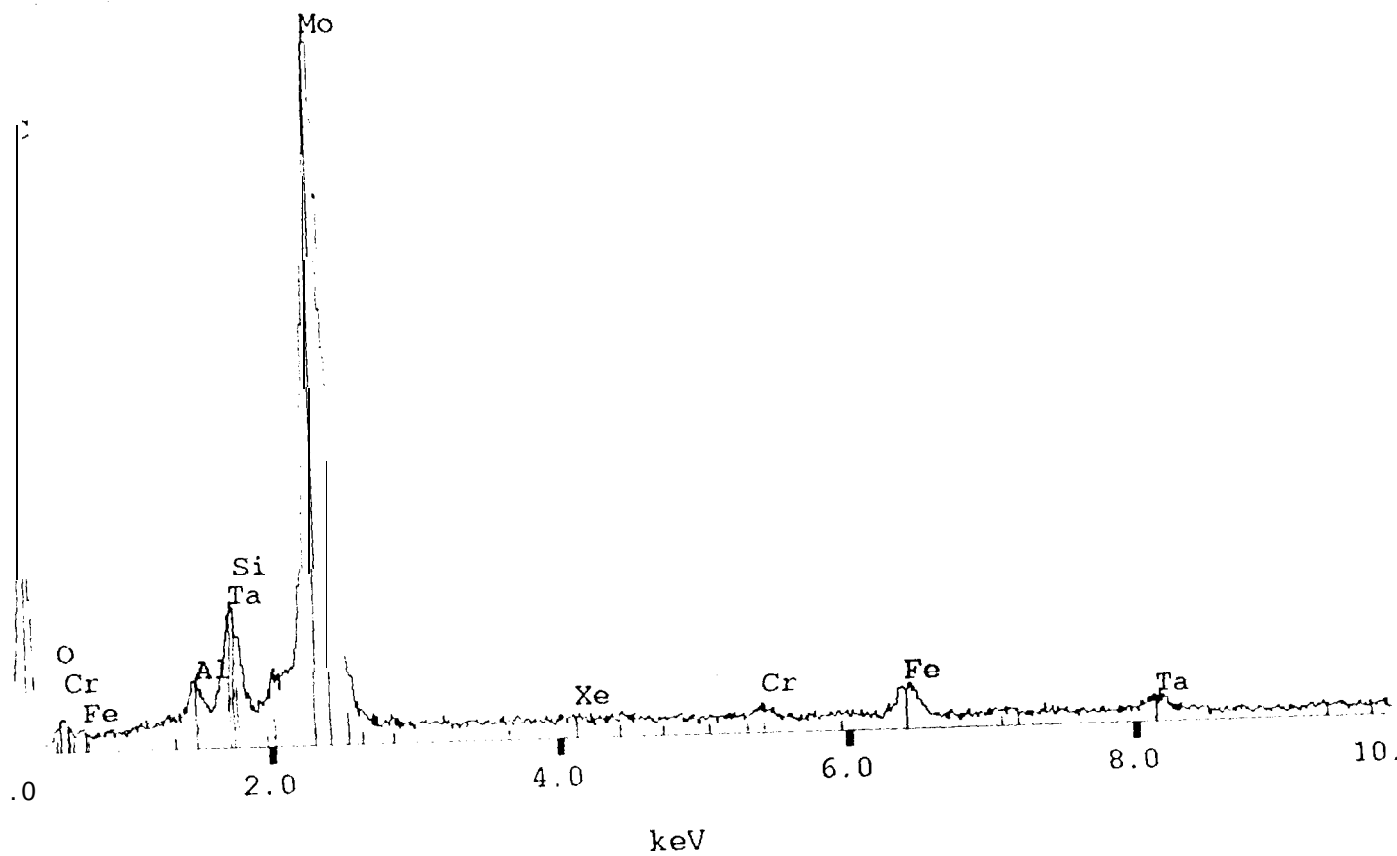
1742 FS

sample

ACCEL C/downstream edge/hole edge

sample

ACCEL C/downstream edge/webbing surface



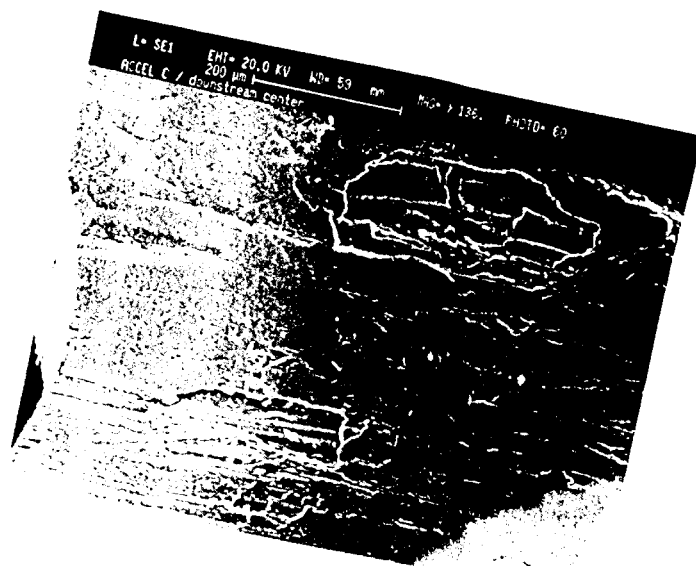


Fig 40



Fig 41

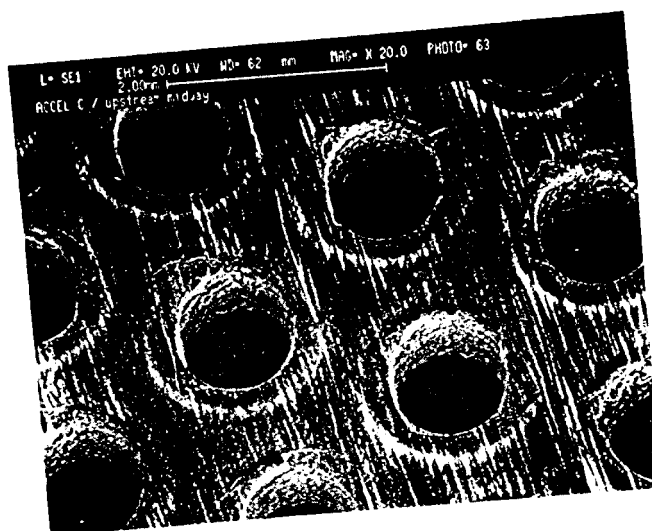


Fig 42

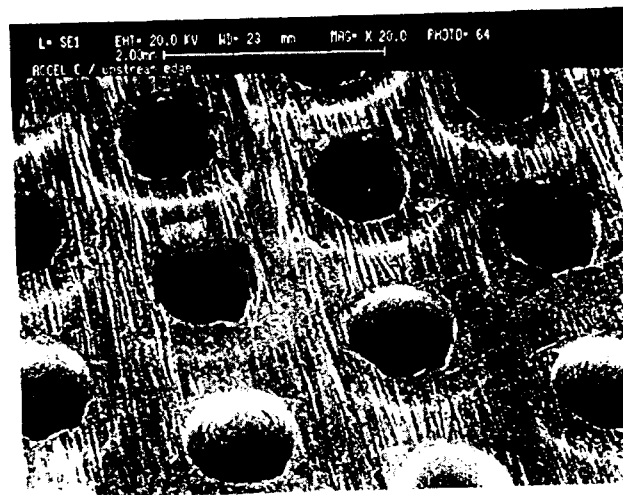


Fig 43

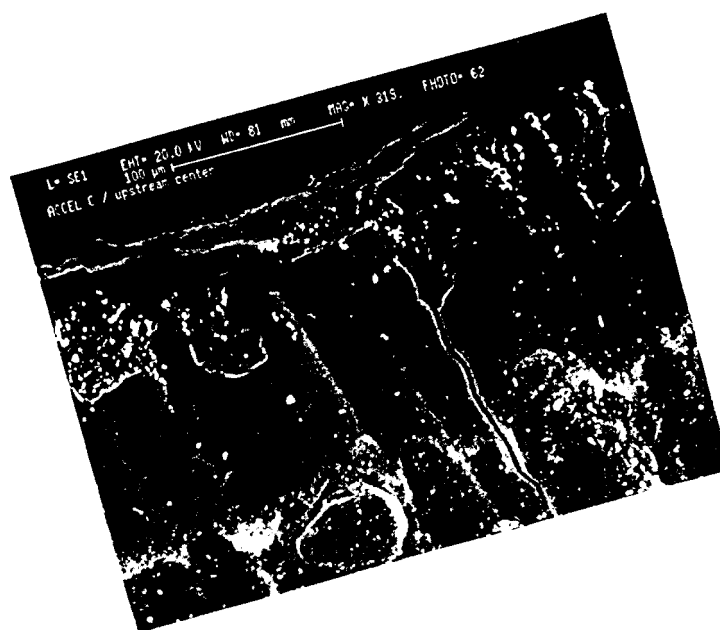


Fig 44

ACCEL C UPSTREAM BEND AROUND HOLE

Fig 48 45

X-ray Display 1

10 spectra selected

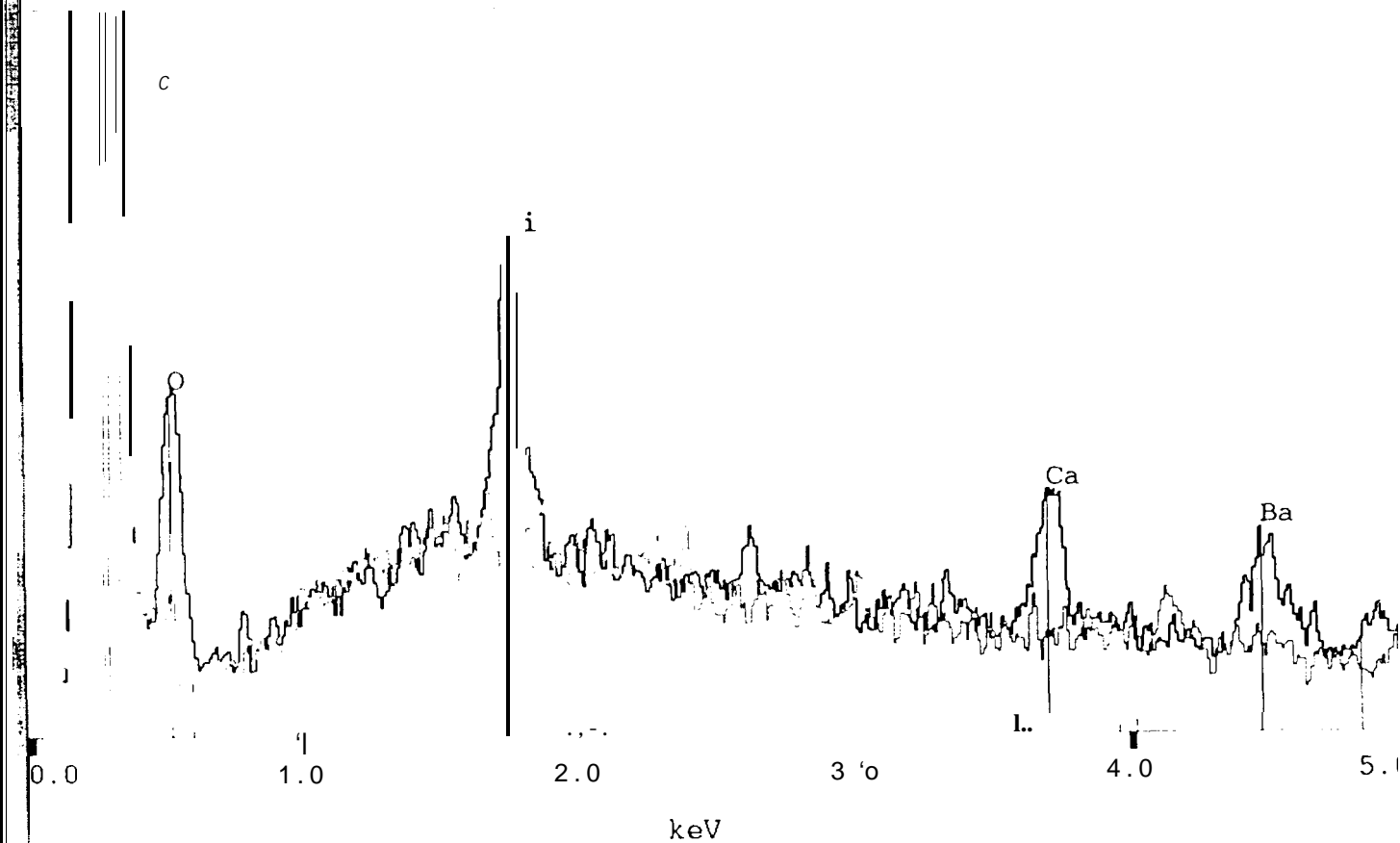
109 FS

✓ sample

ACCEL C/upstream edge/band around hole

✓ sample

ACCEL C/upstream edge/near hole



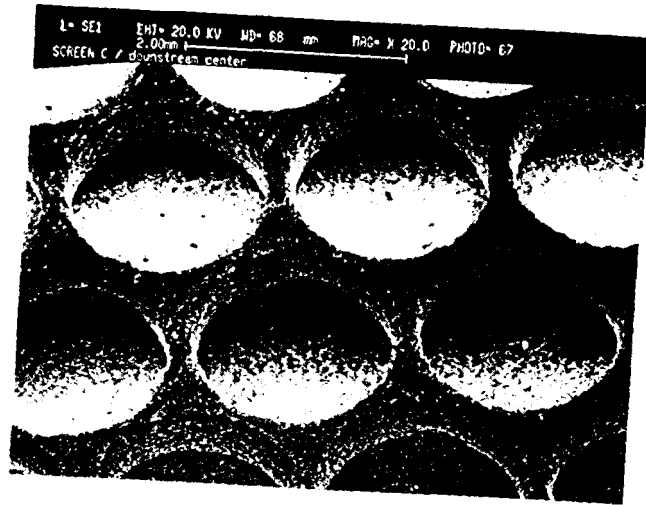


Fig 46

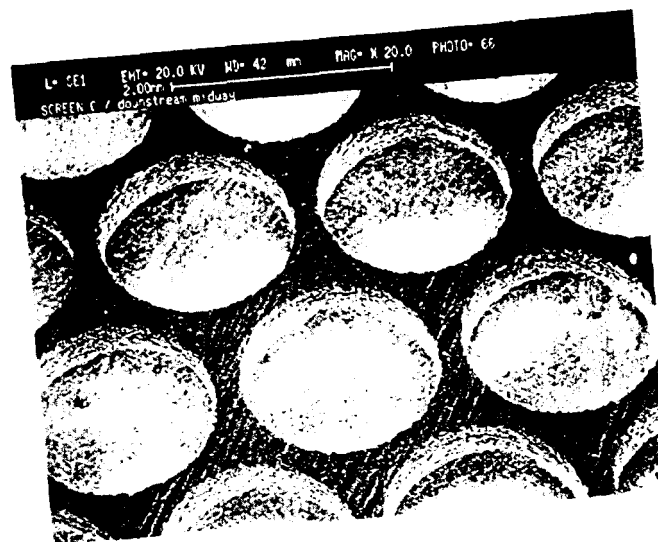


Fig 47

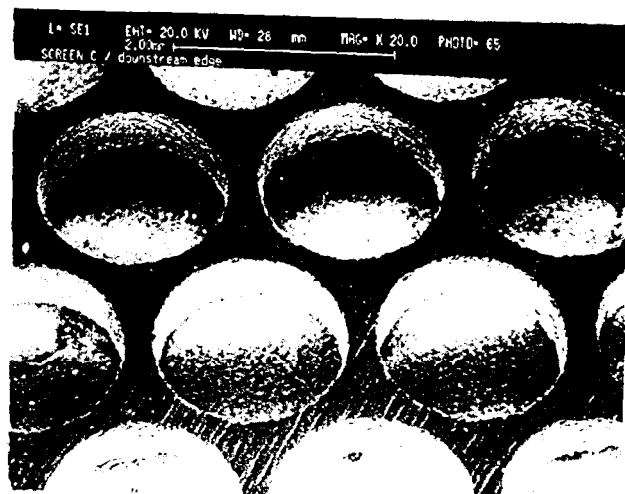


Fig 48

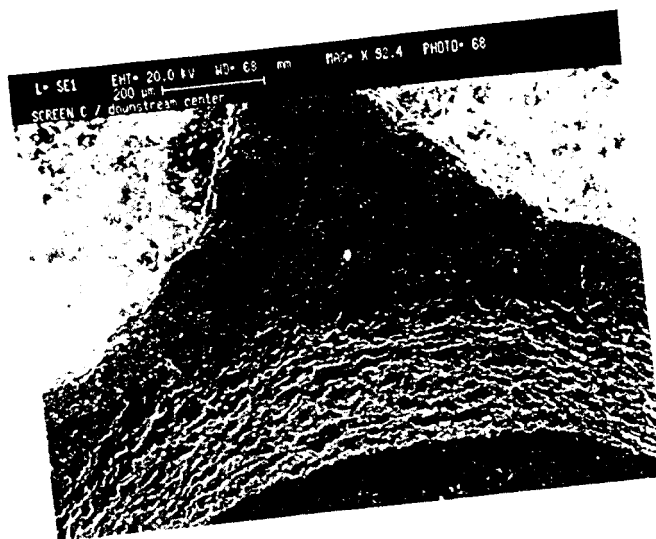


Fig 49

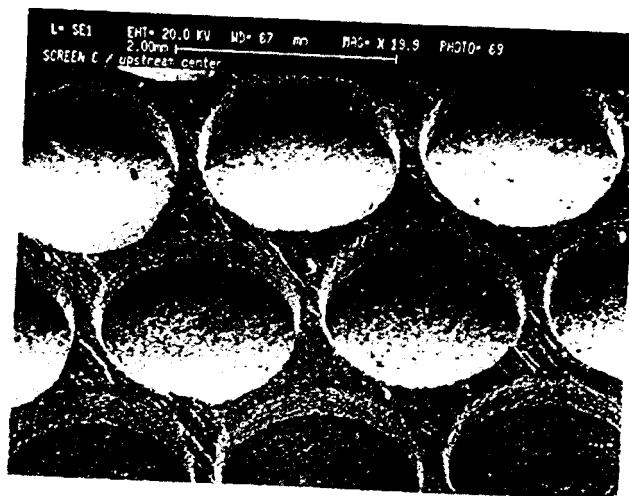
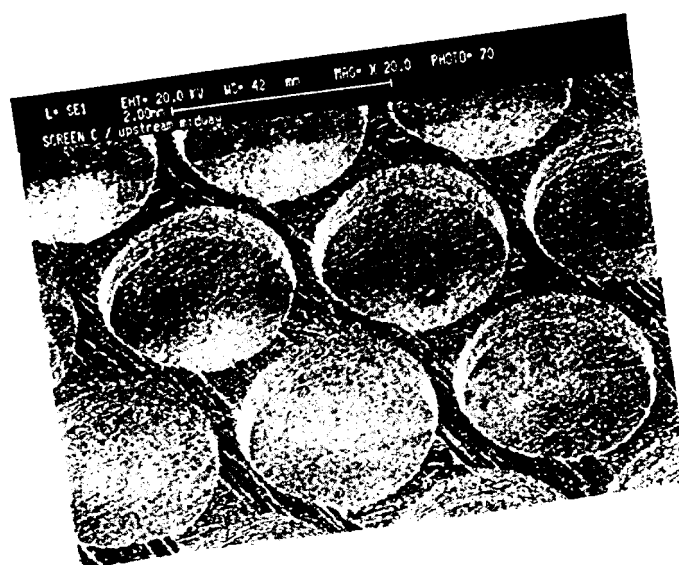


Fig 50



156

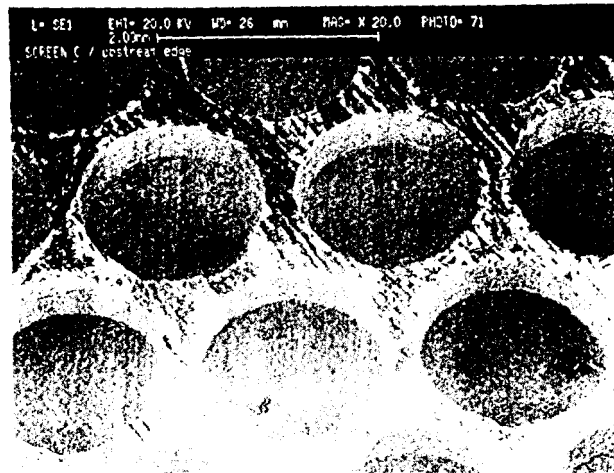


Fig 52

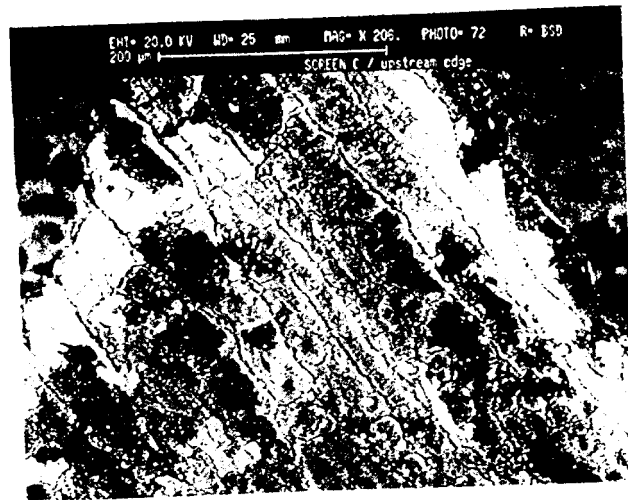
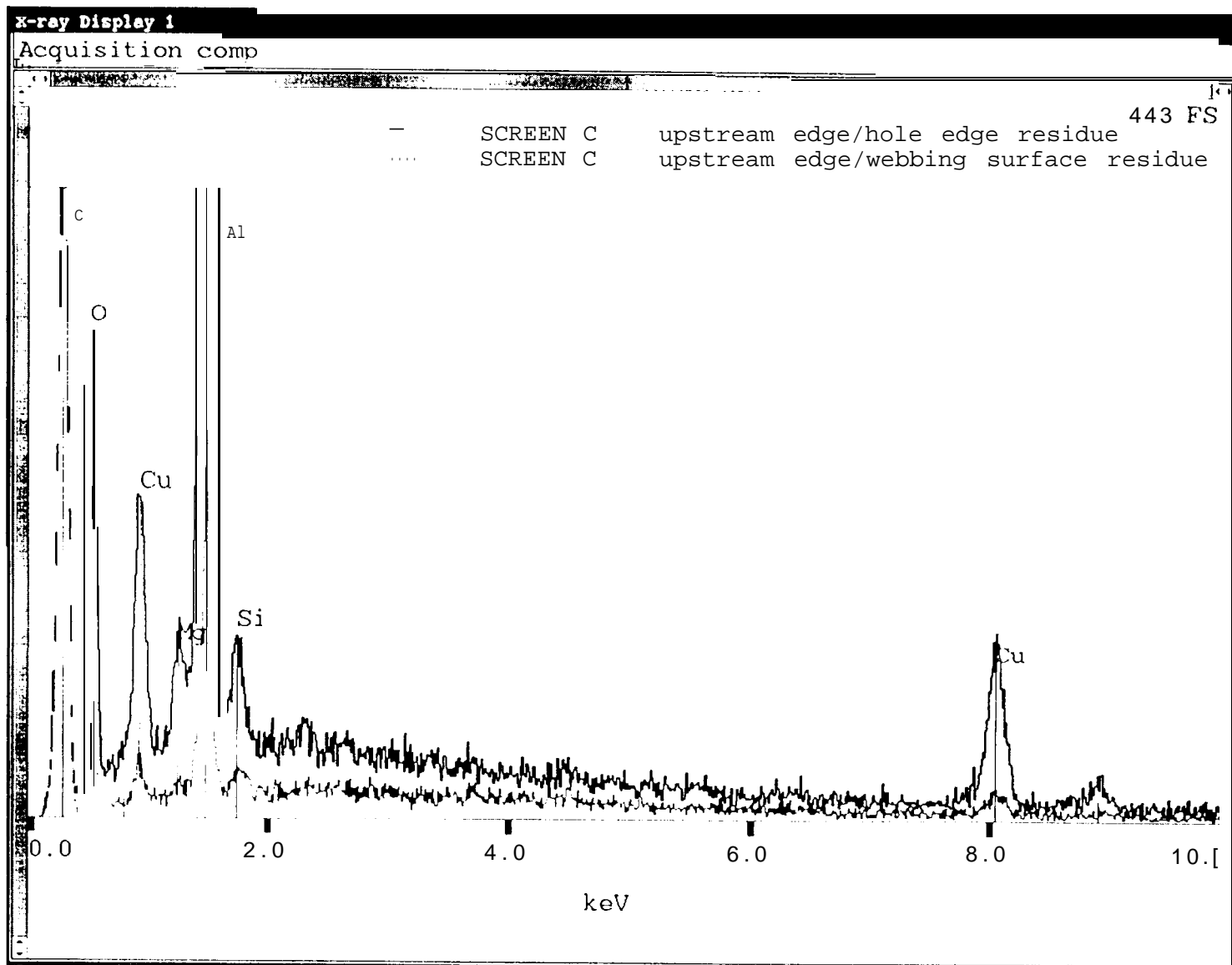


Fig 53

SCREEN C , UPSTREAM EDGE DEPOSITS

Fig 54



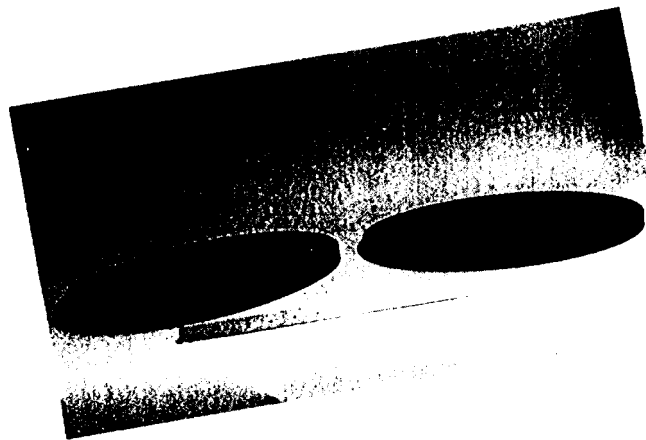


Fig 56

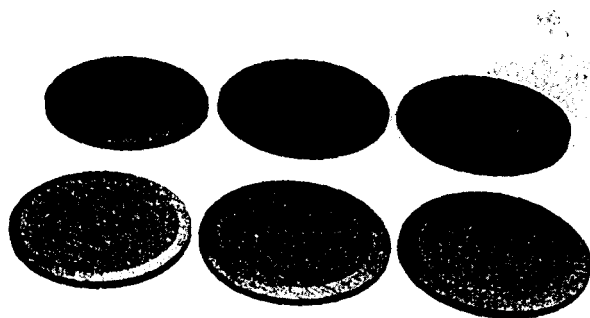


Fig 58

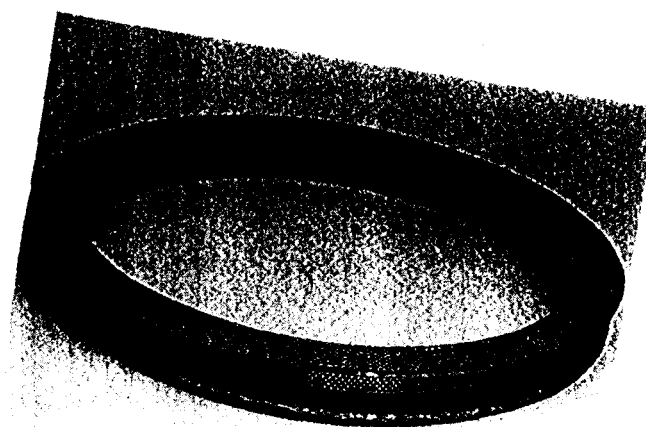


Fig 59

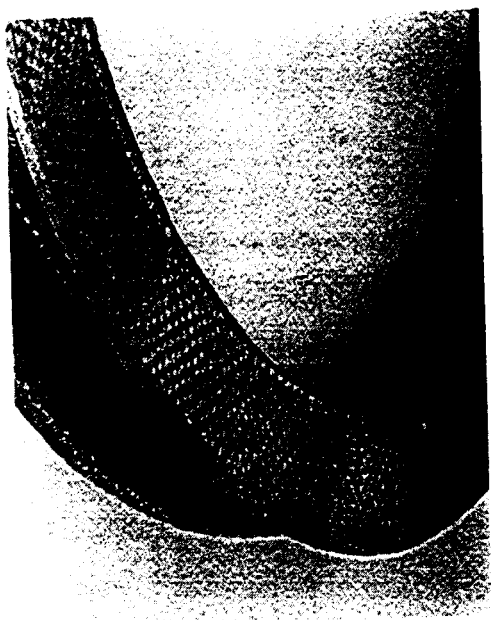


Fig. 60

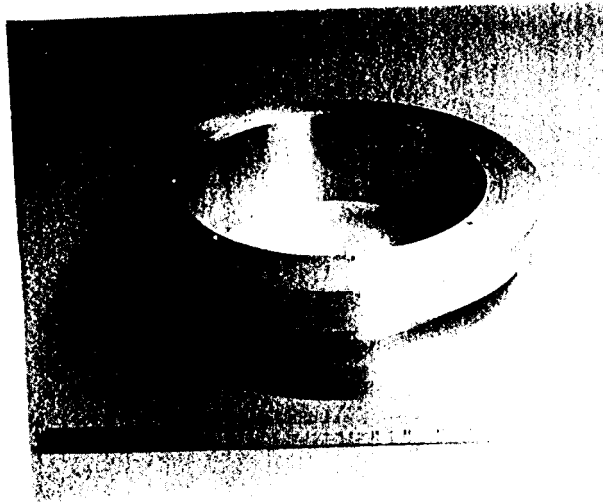


Fig 61

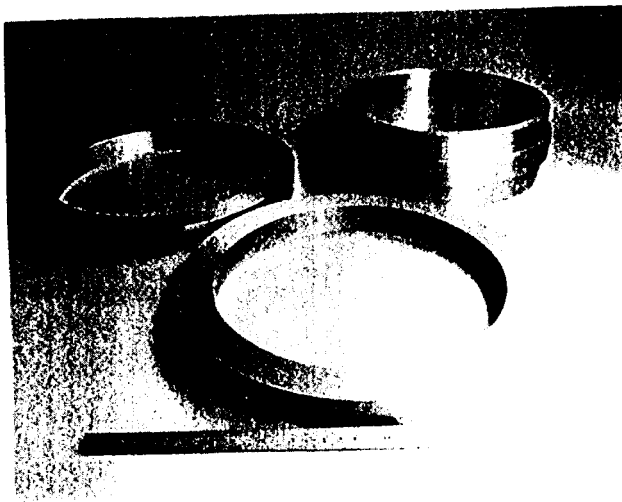


Fig 62